

**An Automatic System for Hyperspectral Remote Sensing
Endmember Unmixing**

By

Tian Han


B.Sc., Ocean University of Qingdao, China, 1984

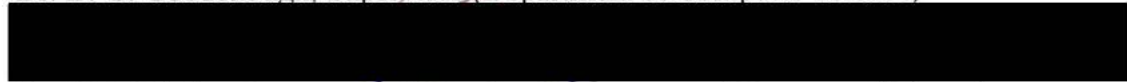
A Thesis Submitted in Partial Fulfillment of the
Requirements for the Degree of


Master of Science

In the Department of Computer Science

We accept this thesis as conforming
to the required standard


Dr. D. G. Goodenough, Supervisor (Department of Computer Science)


Dr. J. H. Jahnke, Departmental Member (Department of Computer Science)


Dr. K. O. Niemann, Outside Member (Department of Geography)


Dr. H. Zwick, External Examiner (MacDonald Dettwiler, and Associates Ltd.)

© Tian Han, 2003
University of Victoria


All rights reserved. This thesis may not be reproduced in whole or in part, by photocopy or other means, without the permission of the author.

Supervisor: Dr. D. G. Goodenough

Abstract

Subpixel information on the components within a pixel is usually desired for remote sensing imagery produced by the medium resolution (30m) sensors. This information includes the number of endmembers in the image scene, endmember spectra, and the endmember fractions for each of the image pixels. With its property of high spectral and relatively low spatial resolution, hyperspectral imagery provides us a perfect data source to explore subpixel information with linear spectral unmixing techniques. In this thesis, linear spectral unmixing algorithms are classified according to whether one is considering the unmixing constraints or requiring all endmembers as *a priori*. Two algorithms are analyzed and extended for endmember extraction and unmixing. The endmember extraction algorithm is developed based on the unconstrained least squares regression, while the unmixing algorithms are derived from the constrained energy minimization and constrained least squares regression, respectively. These algorithms are implemented in the IDL language and tested with both simulated and real hyperspectral data. The computed result shows a very good agreement with the truth data. The accuracy is within 2% for simulated data and reasonable for the real data.


Dr. D. G. Goodenough, Supervisor (Department of Computer Science)


Dr. J. H. Jahnke, Departmental Member (Department of Computer Science)


Dr. K. O. Niemann, Outside Member (Department of Geography)


Dr. H. Zwick, External Examiner (MacDonald Dettwiler, and Associates Ltd.)

Table of Contents

Abstract	ii
Table of Contents	iii
List of Tables	v
List of Figures	vi
Acknowledgements	viii
Chapter 1 Introduction	1
Chapter 2 Concept and Background of Hyperspectral Remote Sensing Technology	4
2.1 Imaging Spectrometry	4
2.2 Hyperspectral and Multispectral Remote Sensing	7
2.3 Challenges and Impacts of Hyperspectral Imagery	10
Chapter 3 Linear Spectral Unmixing	12
3.1 Background and Concept of Spectral Unmixing	12
3.2 Linear Spectral Unmixing Modeling	14
3.3 Variants of Linear Spectral Unmixing	16
Chapter 4 An Unsupervised And Unconstrained Linear Spectral Unmixing Algorithm Based on Localized Constrained Energy Minimization	18
4.1 Constrained Energy Minimization	18
4.2 Operator Derivation of the Constrained Energy Minimization.....	20
4.3 Implementation Issue and Localized Constrained Energy Minimization	21
4.4 Algorithm Efficiency Analysis	26
Chapter 5 An Unsupervised and Fully Constrained Linear Spectral Unmixing Algorithm Based on Fully Constrained Least Squares Estimation	28
5.1 Supervised Linear Spectral Unmixing and Fully Constrained Least Squares	28
5.2 Algorithm for Solving Fully Constrained Least Squares Problems	29
5.3 Algorithm for Direct Endmember Extraction	32
5.4 Implementation Issues and Algorithm Efficiency	34
Chapter 6 Validation of Spectral Unmixing Results	38
6.1 Test Site and Field Data Acquisition	38
6.2 Validation of Results from Localized Constrained Energy Spectral Unmixing Algorithm	40

6.2.1 Validation with Simulated Hyperspectral Data	40
6.2.2 Validation with Hyperion Data	46
6.2.3 Validation with AVIRIS Data	49
6.3 Validation of Results from Fully Constrained Least Squares Spectral Unmixing Algorithm	51
6.3.1 Validation with Simulated Hyperspectral Data	51
6.3.2 Validation with Hyperion Data	54
6.3.3 Validation with AVIRIS Data	56
Chapter 7 Hyperspectral Unmixing Software Development	58
7.1 Limitations of Current Commercial Spectral Unmixing Software	58
7.2 Programming language	60
7.3 Software Development	61
Chapter 8 Conclusions And Future Work	66
Bibliography	70
Appendix A Specifications of AVIRIS Image	75
Appendix B Specifications of Hyperion Image	76
Appendix C Hyperion Data Preprocessing	77

List of Tables

Table 6.1 Comparison between Real and Computed Results by Constrained Energy Minimization Spectral Unmixing Algorithm	44
Table 6.2 Comparison between Real and Computed Results by Localized Constrained Energy Minimization Spectral Unmixing Algorithm	45
Table 6.3 Result Comparison between Localized Constrained Energy Minimization Spectral Unmixing and Spectral Angle Mapper Classification with Hyperion Data.....	49
Table 6.4 Result Comparison between Localized Constrained Energy Minimization Spectral Unmixing and Spectral Angle Mapper Classification with AVIRIS Data.....	49
Table 6.5 Compositions of Simulated Pixels	51
Table 6.6 Comparison between Real and Computed Results by Fully Constrained Least Squares Spectral Unmixing Algorithm.....	54
Table 6.7 Result Comparison between Fully Constrained Least Squares Spectral Unmixing and Spectral Angle Mapper Classification with Hyperion Data	56
Table 6.8 Result Comparison between Fully Constrained Least Squares Spectral Unmixing and Spectral Angle Mapper Classification with AVIRIS Data.....	57
Table 8.1 Linear Spectral Unmixing Cases.....	65

List of Figures

Figure 2.1 Concept of Hyperspectral Imagery	5
Figure 2.2 AVIRIS Image Cube	6
Figure 2.3 Hyperion Image Cube	6
Figure 2.4 TM Image Cube	8
Figure 2.5 Multispectral and Hyperspectral Profiles	9
Figure 3.1 Illustration of Spectral Unmixing	14
Figure 4.1 Flow Chart of Localized Constrained Energy Minimization Spectral Unmixing Algorithm	25
Figure 5.1 Flow Chart of Endmember Extraction Algorithm	35
Figure 5.2 Flow Chart of Fully Constrained Least Squares Spectral Unmixing Algorithm	36
Figure 6.1 Test Site and Field Data Acquisition	39
Figure 6.2 Endmember material ((a) Douglas-fir, (b) Grass, (c) Water, (d) Salal, and (e) Soil.....	41
Figure 6.3 Target Spectra in Reflectance	42
Figure 6.4 Examples of the Simulated Hyperspectral Data for Testing Constrained Energy Minimization Spectral Unmixing Algorithm.....	42
Figure 6.5 Simulated Endmember Fractions Detected by Constrained Energy Minimization Spectral Unmixing Algorithm	43
Figure 6.6 Simulated Endmember Fractions Detected by Localized Constrained Energy Minimization Spectral Unmixing Algorithm	45
Figure 6.7 Hyperion Endmember Spectra in Radiance Extracted from Image.....	47
Figure 6.8 Hyperion Endmember Fraction Images Created by Localized Constrained Energy Minimization Spectral Unmixing Algorithm	47
Figure 6.9 Classification Results by Spectral Angle Mapper	48
Figure 6.10 AVIRIS Endmember Fraction Images Created by Localized Constrained Energy Minimization Spectral Unmixing Algorithm	50
Figure 6.11 Examples of Simulated Hyperspectral Data for Testing Fully Constrained Least Squares Spectral Unmixing Algorithm	52

Figure 6.12 Simulated Endmember Spectra Detected by Fully Constrained Least Squares Spectral Unmixing Algorithm	52
Figure 6.13 Simulated Endmember Fractions Detected by Fully Constrained Least Squares Spectral Unmixing Algorithm.....	53
Figure 6.14 Hyperion Endmember Spectra Detected by Fully Constrained Least Squares Spectral Unmixing Algorithm	54
Figure 6.15 Hyperion Endmember Fraction Images Created by Fully Constrained Least Squares Spectral Unmixing Algorithm	55
Figure 6.16 Endmember Spectra Extracted from AVIRIS Image by Fully Constrained Least Squares Spectral Unmixing Algorithm	56
Figure 6.17 AVIRIS Endmember Fraction Images Created by Fully Constrained Least Squares Spectral Unmixing Algorithm	57
Figure 7.1 Image and Endmember Spectrum Input GUI	62
Figure 7.2 Endmember Display and Unmixing Method Selection GUI.....	63
Figure 7.3 Program Block Diagram	64

Acknowledgements

I would like to give my sincere gratitude to my thesis adviser, Dr. David Goodenough, for his invaluable guidance, encouragement, and support throughout my graduate work, who opened the door for me to the fascinating world of digital remote sensing. I would like to thank Dr. Olaf Niemann and Dr. Jens Jahnke for agreeing to serve on my thesis committee and for their invaluable suggestions and constructive criticisms. Finally, I would to express my gratitude to my wife Jing and my son Mike for their loving support.

Chapter 1

Introduction

Hyperspectral remote sensing, or imaging spectrometry, from both airborne and spaceborne platforms has become a very useful tool for information extraction and ground target detection [16]. With the high spectral resolution of the hyperspectral remote sensing imagery we are able to obtain contiguous spectral distributions to distinguish the components of a spectrum, and hence to detect and recognize the corresponding material on the ground. This ability has many applications. For example, hyperspectral remote sensing produces information on forest species, stand density, and canopy chemistry in forest applications, automatic target detection and recognition in military applications, acid rain and mountain fire damage assessment in environmental applications, crop identification and yield estimation, etc. .

Hyperspectral imagery, however, usually has coarse spatial resolution. For example, the spatial resolution of high elevation U-2 airborne AVIRIS imagery is about 20-meters. This means that each AVIRIS pixel represents a 20m-by-20m area on the ground. Different materials may occur in this area. In this case, the spectral signature of each pixel is a mixture of the individual material signatures contained within the pixel [28]. A pixel that has this characteristic is called a mixed pixel, and each material spectrum contained within the pixel is termed an endmember signature, which occurs at the subpixel level. This subpixel mixture proposes a challenge, which cannot be properly solved by the traditional pixel-based methodology of the current commercially available remote sensing software.

The research question of this thesis is, how do we unmixing hyperspectral pixels to determine the fractions of endmember signatures, which correspond to proportions of endmember materials in the corresponding area on the ground? Based on the research question, the thesis is to introduce, improve, and implement two linear spectral unmixing algorithms. The first algorithm is based on the theory of the Constraint Energy Minimization (CEM), which is usually used to detect and estimate the direction of arrival of multiple radio-frequency signals that are collected simultaneously by a multi-element antenna array [8]. The second algorithm is derived from constrained least squares regression, which turns the spectral unmixing problem into a least squares estimation with constraints on the unmixing result [7]. The algorithms are then designed and implemented to generate a spectral unmixing software package, which is used for the hyperspectral endmember detection and classification. For testing and result validation simulated hyperspectral data, generated from field spectrometer measurements, are used. These are followed by testing of these algorithms on real images of AVIRIS (airborne) and Hyperion (satellite), taken over the Greater Victoria Watershed (GVWD) on Vancouver Island, British Columbia, Canada.

Two goals are expected for this study. The first goal is to demonstrate that the implemented algorithms can correctly process the hyperspectral data, identify correctly endmember targets, and generate endmember abundance proportional images. The second goal is to develop a software package for automatic hyperspectral endmember detection and classification.

The thesis is organized as follows. Chapter 2 provides the background on hyperspectral imaging spectrometry, which includes AVIRIS and Hyperion sensors as two examples. The advantages of hyperspectral over multispectral data are illustrated. The issues generated by hyperspectral data processing are also included in this Chapter. The formulation of the hyperspectral unmixing problem is discussed in Chapter 3. The description of linear spectral unmixing models, mathematical expressions, and many of the variants are also covered in this chapter. In Chapter 4, the Constrained Energy Minimization (CEM) algorithm is introduced, including the origin of CEM, mathematical derivation of CEM, and the improvements in this thesis on the original CEM. Noting the unconstrained nature of the CEM, an unsupervised constrained spectral unmixing algorithm based on the fully constrained least squares (FCLS) method is discussed in Chapter 5. The correctness and effectiveness of the hyperspectral unmixing algorithms based on CEM and FCLS are tested and validated with both simulated and real hyperspectral images in Chapter 6. Several issues are discussed in Chapter 7, related to the restrictions of current commercial spectral unmixing software, programming language selection, and the software development for automatic spectral unmixing. Finally, in Chapter 8 concluding remarks are provided and the areas for continued research in the future are identified. Three appendices give the detailed information about AVIRIS data, Hyperion data, and Hyperion data radiometric correction methods.

Chapter 2

Concepts and Background of Hyperspectral Remote Sensing

In this chapter, concepts and background information regarding hyperspectral imaging spectrometry, typical hyperspectral remote sensing systems and their specifications, and advantages of hyperspectral remote sensing over multispectral remote sensing are provided. Hyperspectral data challenge the methodologies and algorithms for traditional remote sensing data processing, which were developed primarily for multispectral remote sensing technology. The intention in this chapter is to show the differences between hyperspectral and multispectral remote sensing technology, what can be done with the hyperspectral data, and the necessity to invent new methodologies and algorithms for the hyperspectral data processing.

2.1 Imaging Spectrometry

Imaging spectrometry refers to the imaging of a scene by a large number of discrete, contiguous spectral bands or channels such that a complete reflectance spectrum can be obtained for the region being imaged [37]. These bands cover blue (350 nm) to short-wave infrared wavelengths (2500 nm) of the electromagnetic spectrum. This type of imaging is also known as hyperspectral imaging. The hyperspectral data or imagery are acquired by airborne or spaceborne imaging spectrometers, which simultaneously collect solar energy that is reflected from the surface of the earth and disperse it to hundreds of narrow and contiguous spectral bands [32]. A hyperspectral image can be thought of as an image cube, which is composed of a stack of individual band images. The number of

band images corresponds to the number of spectral bands used by the imaging spectrometer. As shown in Figure 2.1, each pixel in a hyperspectral image is an observation vector, whose elements represent the reflected energy corresponding to each wavelength within the spatial area covered by the pixel. These vectors are often expressed in two-dimensional graphs with X-axis representing wavelength and Y-axis

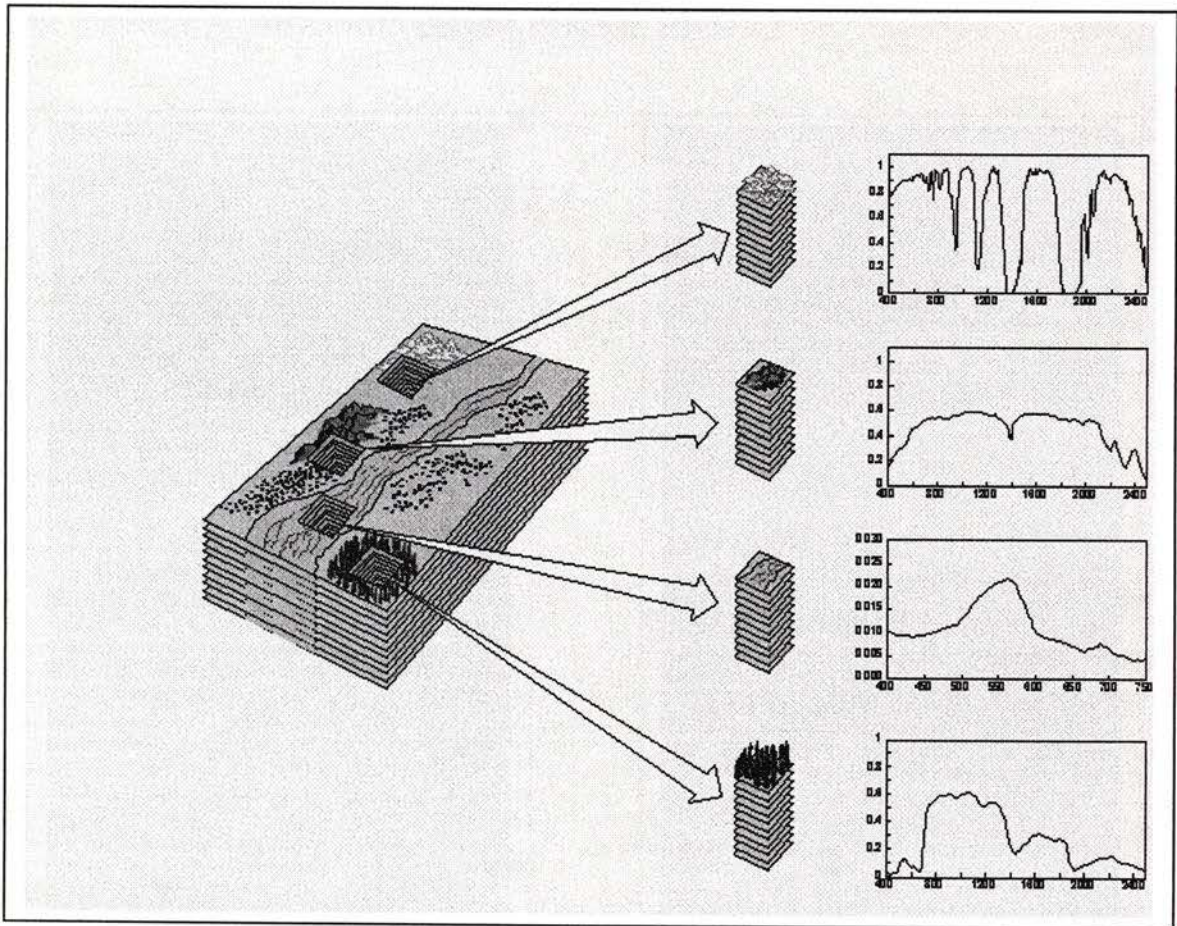


Figure 2.1 Concept of Hyperspectral Imagery

representing the reflected energy. The remote sensing term for such a graph is spectral profile, which can be used for ground material or target identification.

An example of the hyperspectral imaging system is the Airborne Visible/Infrared Imaging Spectrometer (AVIRIS), which was developed at the Jet Propulsion Laboratory (JPL) of NASA. AVIRIS usually flies on the ER-2 aircraft at an elevation of 20,000 meters to measure the total upwelling spectral radiance in the solar-reflected spectrum from 400 to 2500 nm at 10 nm interval in 224 bands [37]. At this elevation, the spatial resolution is approximately 20 meters. For the detail information about AVIRIS system, see Appendix A. An AVIRIS image is shown in Figure 2.2.



Figure 2.2 AVIRIS Image Cube

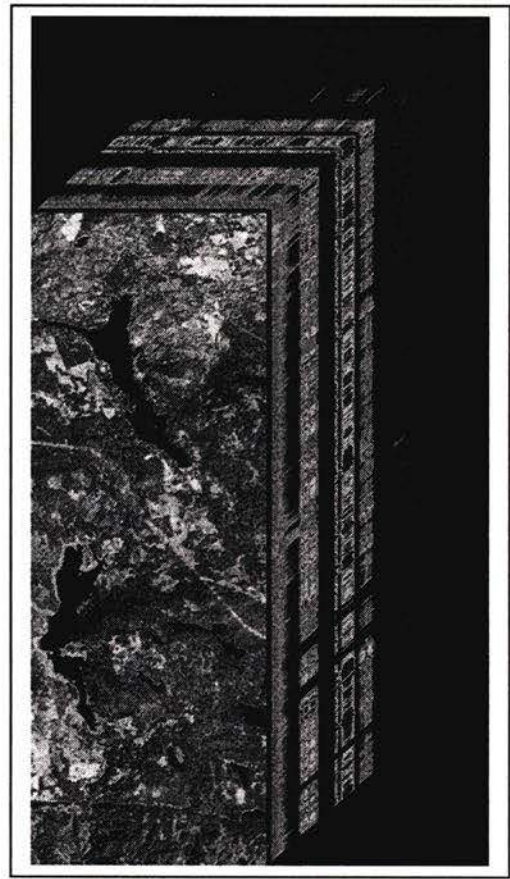


Figure 2.3 Hyperion Image Cube

Another example of a hyperspectral imaging system is the Hyperion, which is a spaceborne sensor onboard the EO-1 satellite, which was launched by NASA on

November 21, 2000 under NASA's New Millennium Program [1]. Hyperion covers a similar range of wavelengths and has similar spectral resolution to AVIRIS. Hyperion has 242 bands with a 30-meter spatial resolution. A Hyperion image is shown in Figure 2.3. See Appendix B for details regarding the Hyperion system.

2.2 Hyperspectral and Multispectral Remote Sensing

The defining characteristic of hyperspectral imagery is its high spectral resolution, which is also its main advantage over multispectral imagery [16]. Compared with a hyperspectral imaging system, a multispectral system measures reflected or emitted energy in several relatively wide and discrete spectral bands. Landsat Thematic Mapper (TM) is a typical sensor for generating multispectral imagery. TM imagery contains 7 bands with 30-meter spatial resolution. The bands are: TM1 (450 – 520 nm, blue), TM2 (520 – 600 nm; green), TM3 (630 – 690 nm, red), TM4 (760 – 900 nm, near infrared), TM5 (1550 – 1750 nm, mid infrared 1), TM6 (10.4 – 12.5 microns, thermal), and TM7 (2080 – 2350 nm, mid infrared 2). Figure 2.4 shows an example of a TM image. The difference between the spectral profiles of multispectral and hyperspectral imagery is apparent (see Figure 2.5). With the spectral information extracted from multispectral images, we are only able to distinguish ground materials with coarse spectral differences, such as water, forest, rock and so on. Hyperspectral imagery provides much finer spectral profiles than that obtainable from multispectral images. Such hyperspectral profiles give the complete description of the spectral response of earth surface materials. This makes it possible to distinguish the land cover materials with subtle spectral

differences, such as different vegetation species, different chemical composition, and water with different levels of visible pollutants. The reflectance spectra of most



Figure 2.4 TM Image Cube

materials on earth's surface contain unique characteristics or diagnostic absorption features [36]. Hyperspectral remote sensing systems being capable of acquiring complete reflectance spectra over a large area offer a powerful tool for the study of the Earth and the environment [31]. Reflectance spectral absorption features, revealed by hyperspectral

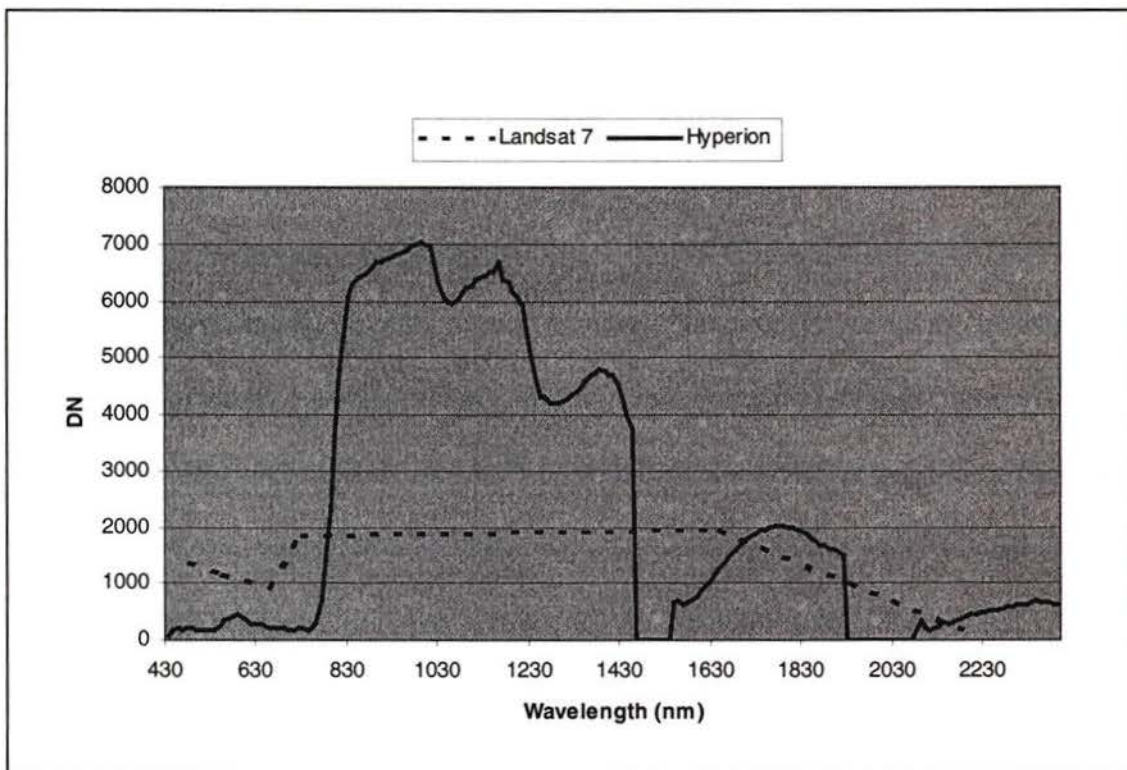


Figure 2.5 Multispectral and Hyperspectral Profiles

remote sensing, can be used to identify minerals by geologists for geologic mapping and studies of volcanoes [27]. For vegetation studies, by employing these spectral features and evaluating the spectral shift of the chlorophyll absorption band, we can determine the effects of soil composition on trees, determine leaf tissue, water content, and assess forest fire damage [31]. Using spectral absorption features, we can also monitor coastal zone regions and other shallow water areas for everything from oil spills and pulp mill effluent to schools of fish [31]. These are only a few examples of the many applications of imaging spectrometry, which are not possible with the multispectral remote sensing.

2.3 Challenges and Impacts of Hyperspectral Imagery

Hyperspectral imagery provides more information and opportunities for the application of remote sensing technology. At the same time, it also brings challenges and impacts, which do not exist in multispectral remote sensing. The direct impact is the tremendous data volume increase. The data volume of a Hyperion image is 35 times the size of a TM image of the same spatial dimension with 8-bit data quantization, because Hyperion has 242 bands, while Landsat TM only has 7. The increased data volume then raises the computational complexity, and hence requires more computing resources. On the other hand, there is a lot of redundancy in hyperspectral data, because of the strong correlation among its band images. This leaves room for data compression. One of the successful lossy hyperspectral data compression algorithms [21] is based on the principal component transformation, which produces a new set of uncorrelated images determined by significant eigenvectors. The original hyperspectral bands are expressed by a linear combination of these uncorrelated images. Because the number of the uncorrelated images is much smaller than the number of the original band images, data compression is achieved.

Hyperspectral imagery also challenges the processing methodologies common to multispectral remote sensing. For example, the availability of enough training pixels is usually not a problem for the supervised classification of multispectral images. However, it is not the case for hyperspectral image classifications. In order to avoid the Hughes phenomenon, (which refers the loss of classifier performance with increasing data

dimensionality when the number of training pixels remains constant [31]), much more training pixels are needed for the supervised hyperspectral image classification, which are expensive to obtain. Getting enough training data for hyperspectral classification is difficult to satisfy in many real situations.

The high spectral resolution of hyperspectral data provides an opportunity to extract subpixel information from remote sensing images. For example, with proper algorithms, it is possible to determine the constituent materials and their proportions of individual pixel areas on the ground. Actually finding subpixel information is a practical question, because most hyperspectral images have relatively low spatial resolution. But the current commercial remote sensing software either does not provide such functionality or is too complicated to be used. The development of new hyperspectral unmixing methodologies and software is needed.

Chapter 3

Linear Spectral Unmixing

The hyperspectral imaging technology provides us opportunities to investigate subpixel information, such as detecting target spectra and computing target abundance proportions. The techniques or algorithms for this purpose are termed as spectral unmixing. In this chapter, the background and concept of spectral unmixing, especially the linear spectral unmixing is introduced. The numerical model of linear spectral unmixing and its variants are also covered. The intention here is to show the theory of spectral unmixing and how to formulate the problem mathematically.

3.1 Background and Concept of Spectral Unmixing

Hyperspectral imagery differs from multispectral imagery by using hundreds of contiguous bands to acquire data, while the latter only uses a few, usually below ten. Hyperspectral imagery, however, often has limited spatial resolution, which implies that each pixel in the image corresponds to an area on the ground where different materials may occur. For example, a Hyperion pixel covers an area of $30\text{ m} \times 30\text{ m}$ on the ground, where there may exist grass, pavement, water, forests, or something else. The high spectral and low spatial resolution of the hyperspectral imagery motivates us to determine the content of each individual pixel. We may ask following questions: What materials exist on the ground covered by a single pixel? What are the abundance fractions of these

materials? Before answering these questions, it is helpful to define and explain several terms related to the spectral unmixing.

- Pure pixel: refers to a pixel, which only consists of one type of ground material.
- Mixed pixel: a pixel covering two or more different types of materials.
- Endmember: refers to the individual material, and sometimes to its spectrum.
- Spectrum or spectral profile: is defined as the reflected energy at different wavelengths, which is usually expressed as a vector and shown as a curve representing the reflected energy corresponding to wavelengths.
- Endmember signature: is the spectral profile of an endmember.
- Pixel signature: refers to a pixel spectral profile, which incorporates the digital numbers (DN) or reflectance extracted from the corresponding image pixel.

Pixels in remote sensing imagery are often mixed pixels. For example, forest pixels seem to only include leaves. They look like pure pixels. But there are many gaps between tree leaves, through which photons penetrate the canopy, hit the soil or tree branches, and then are reflected back to the sensor. Therefore the forest pixels are the mixture of the reflections of leaves, soil, and branches. This indicates that the spectra of these forest pixels are the combination of the endmember signatures of leaves, soil, and branches. The combination happens both linearly and non-linearly, which is dependent on how the endmember materials are mixed and how the electromagnetic energy interacts with them. Considering that the linear combination is dominant in most cases [12], the linear combination is assumed and discussed in this study.

Under this assumption, the spectra extracted from image pixels are then thought of as the linear mixture of the endmembers occurring in the image scene. Mathematically, these mixed pixel spectra are expressed as a linear combination of the endmember spectra [12]. The coefficients for each term of the combination represent the fractional abundance of the corresponding endmembers. This idea is illustrated in Figure 3.1.

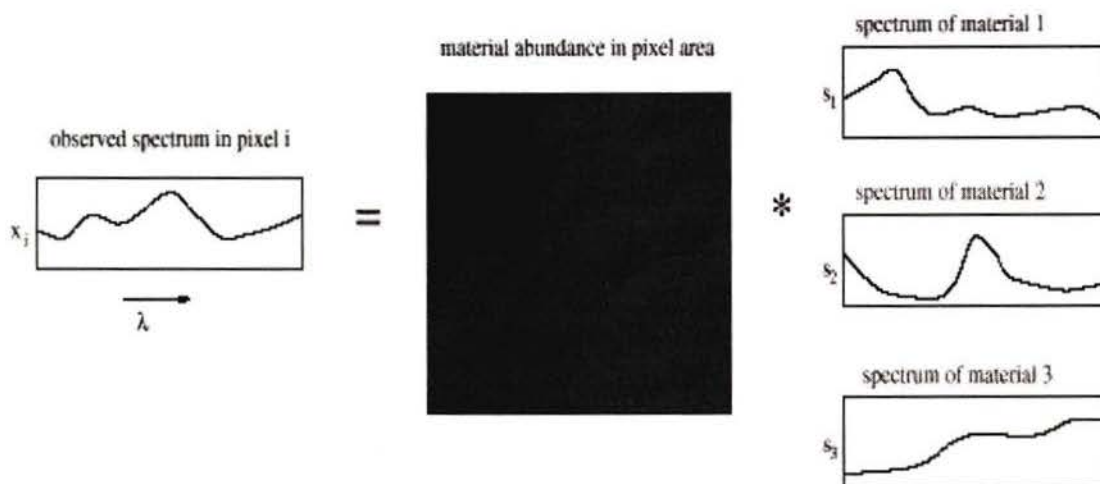


Figure 3.1 Illustration of Spectral Unmixing

3.2 Linear Spectral Unmixing Modeling

Linear spectral unmixing is a widely used approach for remote sensing imagery to determine and quantify multi-components [9]. Since every pixel is acquired at bands with different wavelengths, it is easily represented by a column vector of which each element is a digital number (DN) or reflectance at a particular band. More precisely, let n represent the number of spectral bands. Each pixel of the hyperspectral image, $r(x, y)$, is

a $n \times 1$ column vector, where (x, y) is the spatial position of the pixel. In this case, each hyperspectral pixel is viewed as a point in n dimensional space. Assume that M is the $n \times p$ endmember spectral signature matrix, denoted by $[m_1, m_2, \dots, m_p]$, where m_j is a $n \times 1$ column vector, representing the j th endmember signature resided in the pixel $r(x, y)$, and p is the number of endmembers in the scene. Let $f(x, y) = [f_1, f_2, \dots, f_p]^T$ be a $p \times 1$ abundance column vector associated with $r(x, y)$, where f_j denotes the abundance fraction of the j th endmember presented in the pixel $r(x, y)$. Thus the linear spectral unmixing model is established as follows:

$$r(x, y) = Mf(x, y) + n(x, y) \quad (3.1.1)$$

where $n(x, y)$ is an $n \times 1$ column vector representing the additive random noise, which is assumed to be an independent, identically distributed Gaussian process with zero mean and covariance matrix $\sigma^2 I$, I is the $n \times n$ identity matrix. Therefore, the linear spectral unmixing problem ends up by solving Equation (3.1.1) for $f(x, y)$. In this equation, what we know is $r(x, y)$, which is obtained directly from the given image. M may or may not be known, depending upon whether we have enough *a priori* knowledge about the image scene.

3.3 Variants of Linear Spectral Unmixing

Two constraints on abundance fractions are often considered in linear spectral unmixing.

The first one is called the abundance non-negativity constraint (*ANC*) [9], which

requires all the endmember abundance fractions to be non-negative, i.e. $f_i \geq 0$ for

$i = 1, 2, \dots, p$ in $f(x, y)$. The second one is called abundance sum-to-one constraint

(*ASC*) [9], i.e. $\sum_{i=1}^p f_i = 1$ in $f(x, y)$. These constraints have clear physical meaning.

From the mathematical point of view, in order to solve Equation (3.1.1) for $f(x, y)$, we need to have M *a priori*. However, there is no guaranty for this. The common case is that M is partially known or totally unknown. Depending on whether the constraints are satisfied and whether there is enough *priori* knowledge about the endmember spectrum M , the linear spectral unmixing has the following case variants.

- Case 1 - supervised and unconstrained spectral unmixing. In this case, the unmixing model requires the full knowledge of image scene endmembers, and satisfies neither *ANC* nor *ASC*. This is the most expensive and less realistic case, which is now seldom considered for spectral unmixing.
- Case 2 – supervised and constrained spectral unmixing. With the inclusion of the constraints, this case produces a more optimal unmixing result than the first one. Actually there are two sub-cases depending on whether both constraints (*ANC* and *ASC*) or only one of them are being taken into consideration. If both of them are considered, the case is called fully constrained. Otherwise, the case is called semi-

constrained. A semi-constrained unmixing algorithm, which only considers ANC, was derived in [22], based on non-negativity least squares. The fully constrained algorithm was introduced in [23], and will be discussed in detail in Chapter 5.

- Case 3 – unsupervised and unconstrained spectral unmixing. Though this case does not consider any constraint, it no longer requires endmember spectra to be known in advance. Orthogonal Subspace Projection (OSP) [8] and Constrained Energy Minimization (CEM) are two approaches for this case, of which CEM will be discussed in Chapter 4.
- Case 4 – unsupervised and constrained spectral unmixing. This is the most realistic case, where no endmember information is required and the abundance constraints are fully considered.

Summing up, cases 1 and 2 are supervised models, which rely on the complete knowledge of scene endmember spectra and this is unlikely to happen in reality. We concentrate on cases 3 and 4. These two cases are both unsupervised unmixing variants, which are closer to reality and worthy of being exploited and implemented. In Chapter 4, an unsupervised and unconstrained linear spectral unmixing algorithm (case 3) will be introduced. This algorithm is based on the Constrained Energy Minimization (CEM). Chapter 5 will cover an unsupervised and constrained linear unmixing algorithm (case 4), which is derived from the fully constrained least squares.

Chapter 4

An Unsupervised And Unconstrained Linear Spectral Unmixing Algorithm Based on Localized Constrained Energy Minimization (LCEM_SUA)

In this chapter the focus is on the unsupervised and unconstrained unmixing problem (case 3). The unmixing algorithm, based on the Localized Constrained Energy Minimization (LCEM), is derived and discussed. This algorithm can determine whether a given target or endmember exists or not in an image scene and what its abundance fraction is in each pixel, even though we do not have complete *a priori* knowledge about the image being processed. Because LCEM is derived from the Constrained Energy Minimization (CEM), we start with a brief introduction of CEM.

4.1 Constrained Energy Minimization (CEM)

The Constrained Energy Minimization (CEM) has been studied extensively in the array signal processing community for signal detection, where the signal received by an antenna array is usually a mixture of the desired signal and background signal and noise. The idea of CEM is to keep the desired signal response constant or unity, while suppressing the response of the background signal and noise [8]. In this way the desired signal will stand out from the background signal and noise. This idea is borrowed by the remote sensing community, and is cast into a spectral unmixing algorithm.

Consider a hyperspectral image with s pixels (vectors), (p_1, p_2, \dots, p_s) . Each of them is a column vector and includes the desired spectrum, undesired spectrum, and noise, which correspond to the target signal, background signal, and the noise in signal detection.

What we want is to find out whether the target spectrum exists in each image pixel, and then determine its abundance. For this purpose, we first apply a weighted combining operation to each pixel p_i , $i = 1, 2, \dots, s$, to turn the pixel vector into a scalar value q_i , $i = 1, 2, \dots, s$, which is the weighted sum of the responses at each spectral band within an image pixel. More precisely, q_i can be expressed as

$$q_i = \sum_{j=1}^n w_j (p_i)_j \quad i = 1, 2, \dots, s \quad (4.1.1)$$

where w_j is an element of the column vector $w = (w_1, w_2, \dots, w_b, \dots, w_n)^T$, and n is the number of bands. This is a linear process based on w . In order to make this process meaningful for signal detection or spectral unmixing, it is required that w minimizes the background and noise energy of the signal, while keeping the energy of the target signal at unity. Mathematically, these requirements can be expressed as the following equations.

$$E = \sum_{i=1}^s q_i^2 \quad (4.1.2)$$

$$\sum_{j=1}^n w_j d_j = 1 \quad (4.1.3)$$

where E is the form of the output energy, and d is the target signal or the desired endmember spectrum. Now the signal detection or spectral unmixing problem becomes to determine the operator w , which satisfies Equation 4.1.1, 4.1.2, and 4.1.3.

4.2 Operator Derivation of the Constrained Energy Minimization

In matrix notation, Equation 4.1.1 and 4.1.3 are

$$q_i = w^T p_i \quad i = 1, 2, \dots, s \quad (4.2.1)$$

and

$$w^T d = 1 \quad (4.2.2)$$

Substituting 4.2.1 into 4.1.2, we have the following output energy expression

$$E = \sum_{i=1}^s q_i^2 = \sum_{i=1}^s ((w^T p_i)^T (w^T p_i)) = w^T \left[\sum_{i=1}^s p_i p_i^T \right] w \quad (4.2.3)$$

Combining Equation 4.2.3 and 4.2.2, we see that the signal detection or spectral unmixing turns into the problem of minimizing Equation 4.2.3 under the constraint of Equation (4.2.2), which can be solved by the Lagrange multiplier method [8].

To solve the problem, we construct the constrained cost function

$$J = w^T \left[\sum_{i=1}^s p_i p_i^T \right] w + \lambda (w^T d - 1) \quad (4.2.4)$$

where λ is the Lagrange multiplier. Then by computing the first derivative of the cost function (4.2.4) with respect to w and setting the result to zero, we determine the w , which minimizes the cost function.

$$\frac{\partial J}{\partial w} = \left[\sum_{i=1}^s p_i p_i^T \right] w + \lambda d = 0 \quad (4.2.5)$$

Consider

$$R = \frac{1}{n} \sum_{i=1}^s p_i p_i^T \quad (4.2.6)$$

where R is the covariance matrix of the image without mean removed. For convenience, we just call it the covariance matrix hereafter. Substituting (4.2.6) into (4.2.5), we obtain the following equation

$$\frac{\partial J}{\partial w} = nRw + \lambda d = 0 \quad (4.2.7)$$

Therefore

$$w = kR^{-1}d \quad (4.2.8)$$

where $k = -\frac{\lambda}{n}$. Plugging (4.2.8) into the constraint requirement (4.2.2), we have

$$k = \frac{1}{d^T R^{-1}d} \quad (4.2.9)$$

Substituting k in (4.2.8) with (4.2.9), finally we obtain the CEM operator,

$$w = \frac{R^{-1}d}{d^T R^{-1}d} \quad (4.2.10)$$

which minimizes the undesired spectrum and noise, while keeping the desired spectrum unity. When we apply this operator to a mixed signal or pixel, i.e. $w^T p_i$, ($i = 1, 2, \dots, s$), the background signal or the undesired spectra and noise will be suppressed, while the target signal or spectrum remains unchanged. The result of $w^T p_i$ is a scalar, which represents the abundance fraction of the target spectrum existing in the corresponding pixel [8].

4.3 Implementation Issue and Localized Constrained Energy Minimization

The implementation of the CEM operator (4.2.10) requires calculating the inverse of the image covariance matrix (R^{-1}), and the performance of the CEM operator is largely

dependent on whether we can accurately compute R^{-1} . For a well-conditioned matrix, we can use the standard matrix inversion procedure, such as Gaussian elimination or LU decomposition, to get a fairly accurate result [38]. But the covariance matrix of the hyperspectral data is usually ill conditioned. The reason for this is that many hyperspectral bands are highly correlated. The number of significant eigenvalues of the hyperspectral data is generally less than 10 for Hyperion, while the number of spectral bands is larger than 200. Due to this fact, the ratio of the largest to the smallest eigenvalues, called the condition number, of the correlation matrix is often very large, which causes the accuracy of the inversion of the correlation matrix to deteriorate.

Rather than directly inverting the ill-conditioned hyperspectral covariance matrix, it is better to compute its Singular Value Decomposition (SVD) to determine its numerical rank, eliminate the insignificant eigenvalues, and then compute a pseudoinverse [38].

With the SVD, a $M \times N$ matrix A can be factorized as the product of a $M \times M$ column-orthogonal matrix U , a $M \times N$ matrix Σ , and the transpose of an $N \times N$ orthogonal matrix V , that is

$$A = U \cdot \Sigma \cdot V^T \quad (4.3.1)$$

where

$$\Sigma = \begin{bmatrix} D & 0 \\ 0 & 0 \end{bmatrix}$$

D is a diagonal matrix with non-zero singular values of A as its diagonal entries. The pseudoinverse can be obtained by the inversion of A as follows:

$$A^{-1} \text{ or } (A^+) = V \cdot W^{-1} \cdot U \quad (4.3.2)$$

Ideally the CEM operator should be derived on pixel basis. That is to say, we need to calculate the covariance matrix and invert it for every pixel in the image being processed. This proved to be extremely computing expensive (we'll discuss it later). So the original CEM algorithm [7] used a global covariance matrix, which is the average covariance matrix of the image. In this way the SVD and pseudoinverse are only needed once. Therefore, in the CEM method we assume that the undesired spectrum and noise are completely represented by the single global covariance matrix. Unfortunately this is only true for low spatial frequency images. For an image with high spatial frequency, which is usually the case for real remote sensing imagery, we need to consider the spatial variability. So next we introduce a new approach, which considers the image spatial variability while doesn't dramatically increase the computing cost. This new approach is called the Localized Constraint Energy Minimization (LCEM) method.

LCEM makes a compromise between the computational cost and the local statistical properties. First we separate the image into several image blocks. The size of each image block is dependent on the computing power, the abundance proportion of the target endmember spectrum being unmixed, and the image spatial variability. If the target endmember proportion is low and longer computing time is acceptable, the size of the image block can be smaller. For each image block, separate covariance matrices and pseudoinverses are calculated; and the CEM operator for each block is created. Then we

apply the CEM operators to the pixels within the corresponding image blocks to produce the target endmember abundance fractions.

There is an issue associated with LCEM, for it uses the local covariance matrices to generate CEM operators. The target endmember abundance fractions produced by these operators are not directly comparable. They need to be normalized before they can be used to generate target endmember proportion images. We create a normalization formula (4.3.3) as a common scale that brings different abundance values into a common range,

$$f_i = 1 + \frac{w^T p_i - 1}{1 + d^T p_i / (\|d\| \|p_i\|)} \quad (4.3.3)$$

where f_i is the target endmember fraction after normalization, w the localized CEM operator, d the target endmember spectrum, and p_i a pixel vector. This normalization formula preserves the unity constraint ($w^T d = 1$), and satisfies two implicit requirements. At the extremes, the normalized result reaches the maximum value when the unmixed pixel only contains the target endmember spectrum ($w^T p_i = 1$, thus $f_i = 1$), and reaches the minimum when the unmixed pixel doesn't contain the target spectrum ($w^T p_i = 0$, $d^T p_i = 0$, therefore $f_i = 0$).

Summing up the LCEM derivation and the normalization, we now give the flow chart for implementing the LCEM spectral unmixing algorithm in Figure 4.1.

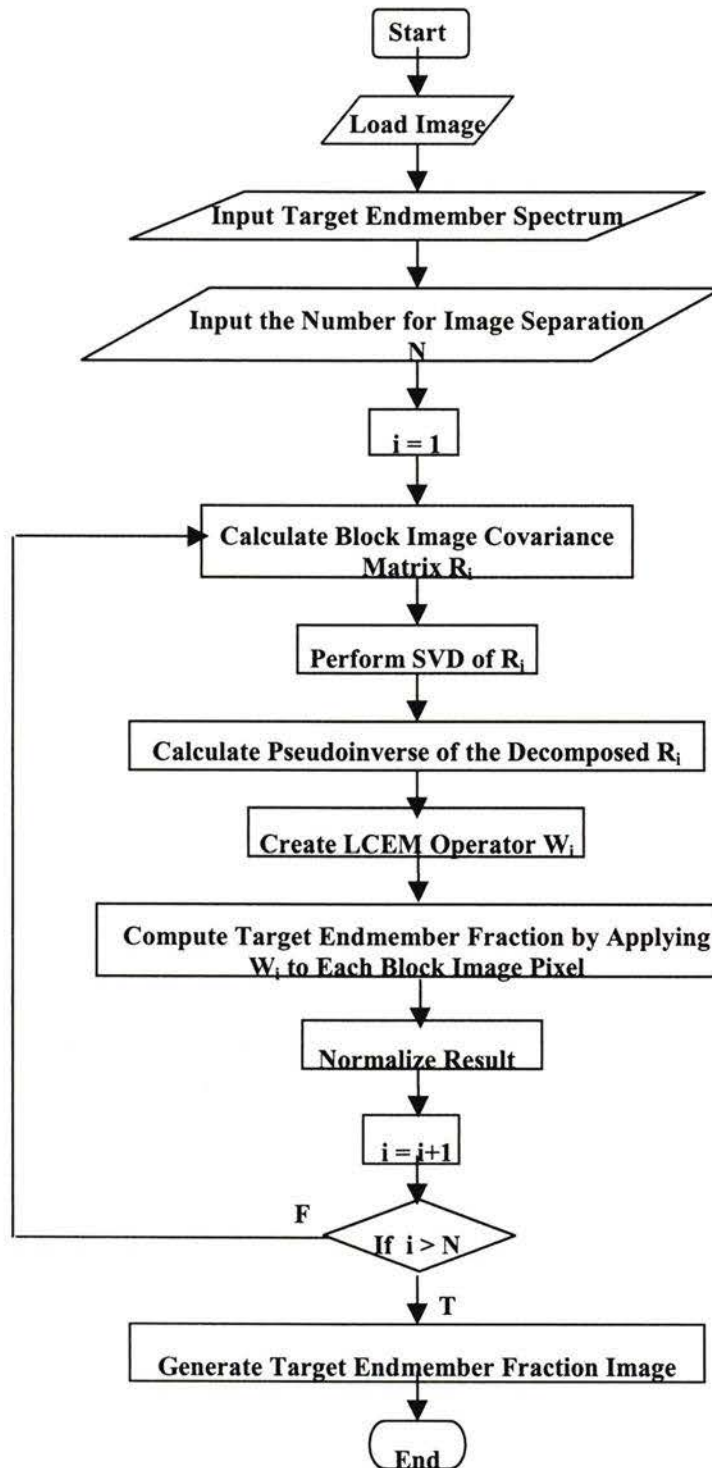


Figure 4.1 Flowchart of Localized Constrained Energy Minimization Spectral Unmixing Algorithm

4.4 Algorithm Efficiency Analysis

The number of floating-point operations (FLOP) required is a standard measure of the efficiency of a numerical algorithm. The CPU time can be estimated by the number of FLOP counts, which are usually given in terms of the problem size, such as the dimension of a matrix. Let us assume the hyperspectral image to be unmixed has n bands and s pixels. The dimension of its covariance matrix is then $n \times n$. To compute the covariance matrix for each pixel, we need n multiplications and $n - 1$ additions. So the covariance matrix of the whole image requires approximately $s \times n$ multiplications and additions. In the big-O notation, this is a $O(n^2)$ problem (for simplicity we assume s and n have the same magnitude). The creation of the CEM operator w requires $2n^2 + n$ multiplications, n divisions, and $5n - 1$ additions, which is also a $O(n^2)$ problem. When applying the CEM operator to each pixel, we end up with a $O(n^3)$ problem. Considering both SVD and pseudoinverse of the image covariance matrix are in $O(n^3)$, the original CEM spectral unmixing is therefore a $O(n^3)$ problem.

For the LCEM, suppose we divide the given image into q blocks. Instead of generating a single covariance matrix as in original CEM, we now generate q matrices, one image block each. The SVD and pseudoinverse are also required to perform q times. Another additional cost is the result normalization, which only requires computing vector inner products and vector norms. For each pixel, this work is in $O(n)$. Because $q \ll s$ and n ,

LCEM is still in the magnitude of $O(n^3)$, even though the cost is about q times more than CEM.

The worst-case scenario is for $q = n$, in which we need to compute the covariance matrix, SVD, and pseudoinverse for each image pixel. Now both SVD and pseudoinverse are in the order of $O(n^4)$, which is very expensive and time consuming. This extreme measure is proved to be effective to process very noisy data (See Chapter 6). Fortunately most hyperspectral data have enough signal-to-noise ratio, so this pixel level CEM is usually not needed for spectral unmixing.

Chapter 5

An Unsupervised and Fully Constrained Linear Spectral Unmixing Algorithm Based on Fully Constrained Least Squares Estimation (FCLS_SUA)

In Chapter 4, a CEM based linear spectral unmixing model was introduced. Because CEM does not consider any constraint requirements, the estimated abundance fractions may not be optimal. Some of them may be less than 0 or greater than 1. In this chapter, we introduce another linear spectral unmixing algorithm, which is based on the fully constrained least squares (FCLS) estimation. In the constrained least squares regression process, we consider both the abundance non-negativity and sum-to-one constraints (ANC and ASC) to improve the optimality of the unmixing result. We start with the supervised and fully constrained linear spectral unmixing and then expand it to the unsupervised version.

5.1 Supervised Linear Spectral Unmixing and Fully Constrained Least Squares

As discussed in Chapter 3, the linear spectral unmixing problem can be expressed as

$$r = Mf \tag{5.1.1}$$

where r is a pixel column vector of the image; M the target spectral signature matrix; f the endmember-abundance-fraction column vector, associated with the pixel r .

Considering the physical meaning of these variables above, there are two implied constraints on f , which are the abundance non-negativity constraint (ANC) and the abundance sum-to-one constraint (ASC). Suppose we know M as *a priori*, (that is why

we call it supervised), and r is obtained from the image, then f can be determined by solving the following linear equations with 2 constraints.

$$\begin{cases} Mf = r \\ \sum_{i=1}^n f_i = 1 \\ f_i \geq 0 \end{cases} \quad \text{for } i = 1, 2, \dots, p \quad (5.1.2)$$

where p corresponds to the number of endmembers resident in the image. Here M is a $n \times p$ matrix, where n represents the number of spectral bands and is usually much larger than p . So the linear system (5.1.2) has more equations, n , than unknowns, p . There is no exact solution to f . What we can get are only the estimates of the exact solution. Therefore, we transform the problem (5.1.2) into a fully constrained least squares problem as follows:

$$\begin{cases} \text{Minimize } \| r - Mf \|^2 \\ \sum_{i=1}^n f_i = 1 \\ f_i \geq 0 \end{cases} \quad \text{for } i = 1, 2, \dots, p \quad (5.1.3)$$

So now the supervised linear spectral unmixing problem is turned into an optimization based on the fully constrained least squares expressed in (5.1.3). The issue is how to solve (5.1.3) for f accurately and efficiently.

5.2 Algorithm for Solving Fully Constrained Least Squares (FCLS) Problem

In this section we focus on how to solve the FCLS problem (5.1.3). There are 2 constraints for (5.1.3), ASC and ANC. If we only considered ASC, the problem could be solved by the standard Lagrange multipliers method in linear programming. In order to

get the optimal result we have to take the second constraint, ANC, into account. But ANC is set of inequalities, which means that the analytic solutions cannot be directly derived from (5.1.3). To work this out, first the ASC is used to generate a Lagrangian cost function, create a steering vector by considering the ANC, find the most invalid result with the help of the steering vectors, and then turn the invalid result into zero [23]. This process is repeated until all the results become valid. At each iteration, M is adjusted accordingly by removing the endmember spectrum, which gives the most invalid result. The method is described in detail below.

We establish the Lagrangian cost function by only considering ASC,

$$J = \frac{1}{2}(r - Mf)^T (r - Mf) + \lambda \left(\sum_{i=1}^n f_i - 1 \right) \quad (5.2.1)$$

where λ is the Lagrange multiplier. Equation (5.2.1) can be written in the following matrix form,

$$J = \frac{1}{2}(r - Mf)^T (r - Mf) + \lambda(f^T v - 1) \quad (5.2.2)$$

where $v = [1, 1, \dots, 1]^T$. Now by differentiating (5.2.2) with respect to f and setting the result to zero, we obtain:

$$\frac{\partial J}{\partial f} = \frac{1}{2} \frac{\partial (r^T r - r^T Mf - f^T M^T r - f^T Mx)}{\partial f} - \lambda v = 0 \quad (5.2.3)$$

This gives:

$$M^T Mf - \lambda v = M^T r \quad (5.2.4)$$

Then we differentiate (5.2.2) with respect to λ and set it to zero, which leads to

$$v^T f = 1 \quad (5.2.5)$$

From Equation (5.2.4), we have

$$f = (M^T M)^{-1} (M^T r + \lambda v) = (M^T M)^{-1} M r + \lambda (M^T M)^{-1} v \quad (5.2.6)$$

As we know that $(M^T M)^{-1} M r$ is the solution to the unconstrained least squares (UCLS) problem ($r = M f$). We denote it as f_{UCLS} . That is

$$f_{UCLS} = (M^T M)^{-1} M r \quad (5.2.7)$$

$$\text{Let } s = (M^T M)^{-1} v \quad (5.2.8)$$

Substituting (5.2.7) and (5.2.8) into (5.2.6), we have

$$f = f_{UCLS} + \lambda s \quad (5.2.9)$$

Equation (5.2.9) shows that the fully constrained least squares solution f is composed of two terms, the unconstrained solution f_{UCLS} and an adjustment term λs . By substituting f in (5.2.5) with (5.2.6), we obtain

$$\lambda = (1 - v^T (M^T M)^{-1} M r) / (v^T (M^T M)^{-1} v) \quad (5.2.10)$$

Equation (5.2.10) is further simplified as

$$\lambda = (1 - v^T f_{UCLS}) / (v^T s) \quad (5.2.11)$$

Now it is clear the FCLS problem (5.1.3) can be solved iteratively through the computation of Equation (5.2.9) and (5.2.11). The key point here is the vector s , which functions as a steering vector to determine the adjustment needed for λ . For each iteration, we divide each negative f_i by its corresponding component in vector s and determine which $|f_i / s_i|$ has the largest value. The determined f_i is the element that requires the most steering. It is then set to zero. The corresponding column in M is removed before being used for the next iteration. When all the elements in f become

none negative, the iteration terminates. Now f is the optimal solution of Equation (5.1.3), which represents the fully constrained spectral unmixing result of the pixel r .

5.3 Algorithm for Direct Endmember Extraction

A supervised linear spectral unmixing algorithm was introduced in section 5.2. Provided we have all endmember spectral information M , we can compute their abundance fractions with this algorithm. But usually we do not have all endmember spectral information for an image. The real situation is that we only have partial or even no knowledge about the endmembers in the image being processed. We need to figure out from the image how many endmembers existed and what the endmember spectra are. We need to find out the endmember spectra and extract them directly from the image and then use the information for spectral unmixing. In this section, an algorithm is developed for this purpose.

In general, an image usually incorporates a few pure pixels and many mixed pixels. The spectra of these pure pixels are the target or endmember spectra in M of Equation (5.1.3), which are the basic components of all the mixed pixels. From the geometric point of view, each image pixel is thought as a vector in a n dimensional space, where n is the number of the image bands. All pixels of the image constitute a subspace of the n dimensional space. The pure pixels are located at the boundaries of the subspace, while the mixed pixels reside among them [4]. The pure pixels are more unique than mixed pixels. Their uniqueness can be measured by distance. The distance between any two

pure pixels is longer than the distance between any two mixed pixels or one pure pixel and one mixed pixel.

The initial candidates of the pure pixels are the brightest and darkest pixels in the image, which have the maximum and minimum length respectively and can be easily calculated with

$$length = r^T r \quad (5.3.1)$$

Once they are found, their spectra are used to generate an initial M . Then we compute the unconstrained least squares estimates (UCLS) f_{UCLS} of each pixel in the image with

$$f_{UCLS} = (M^T M)^{-1} M r \quad (5.3.2)$$

The next step is to compute the distance between $M f_{UCLS}$ and r , and determine the pixel with the longest distance. That is

$$D_{MAX}(r) = (M f_{UCLS} - r)^T (M f_{UCLS} - r) \quad (5.3.3)$$

Because the distance is the maximum, we can expect that the current pixel r is most different from the spectra in M , and hence it is a good candidate as another endmember, which is then added to M to form a new endmember spectral matrix. This process is repeated until the desired number of endmembers is found, or the distance between r and UCLS result is below a pre-set threshold. The number of endmembers existing in an image scene is either determined by *a priori* knowledge or by the dimensionality of the image, which is believed to be the same as the number of endmembers [21]. The image dimensionality is usually estimated by computing the deflection point of the second order derivative of the image eigenvalue versus band number.

5.4 Implementation Issues and Algorithm Efficiency

By combining the algorithm of endmember extraction developed in Section 5.3 and the algorithm for solving fully constrained least squares problem discussed in Section 5.2, we now have the complete algorithm for the unsupervised and fully constrained linear spectral unmixing, which starts with the endmember extraction.

In the endmember extraction process, the main work involves finding the brightest and darkest pixels by computing the pixel vector inner product, solving the unconstrained least squares by computing the product and its pseudoinverse of the endmember spectral matrix and its transpose, and determining the pixel with the largest difference between the UCLS results and the pixel vectors. The detailed steps and computation are given in Figure 5.1.

To analyze the computational complexity of the endmember extraction algorithm, let us assume the hyperspectral image to be processed have s pixels and n bands. Finding the brightest and darkest pixels requires computing the vector product for each pixel

$(r_i^T r_i = \sum_{j=1}^p r_{i,j}^2)$, which needs $n \times s$ multiplications, $n \times s$ additions, and $2s$ comparisons.

This is of order $O(n^2)$ in simplicity. If the number of desired endmembers is p , the dimension of the endmember matrix M is $n \times p$. It has been shown that the UCLS estimation, $(M^T M)^{-1} M r_i$, is an $O(n^3)$ problem. Here the UCLS needs to be calculated repeatedly. The maximum iterations are $p-1$. Because $p \ll s$ or n , the cost for UCLS

is still at $O(n^3)$. In the same way, we see that computing the differences between UCLS estimates and pixel vectors, $(Mf_{UCLS} - r_i)^T (Mf_{UCLS} - r_i)$, requires $s \times (n \times p + n)$ multiplications, $s \times n$ additions, s comparisons, and

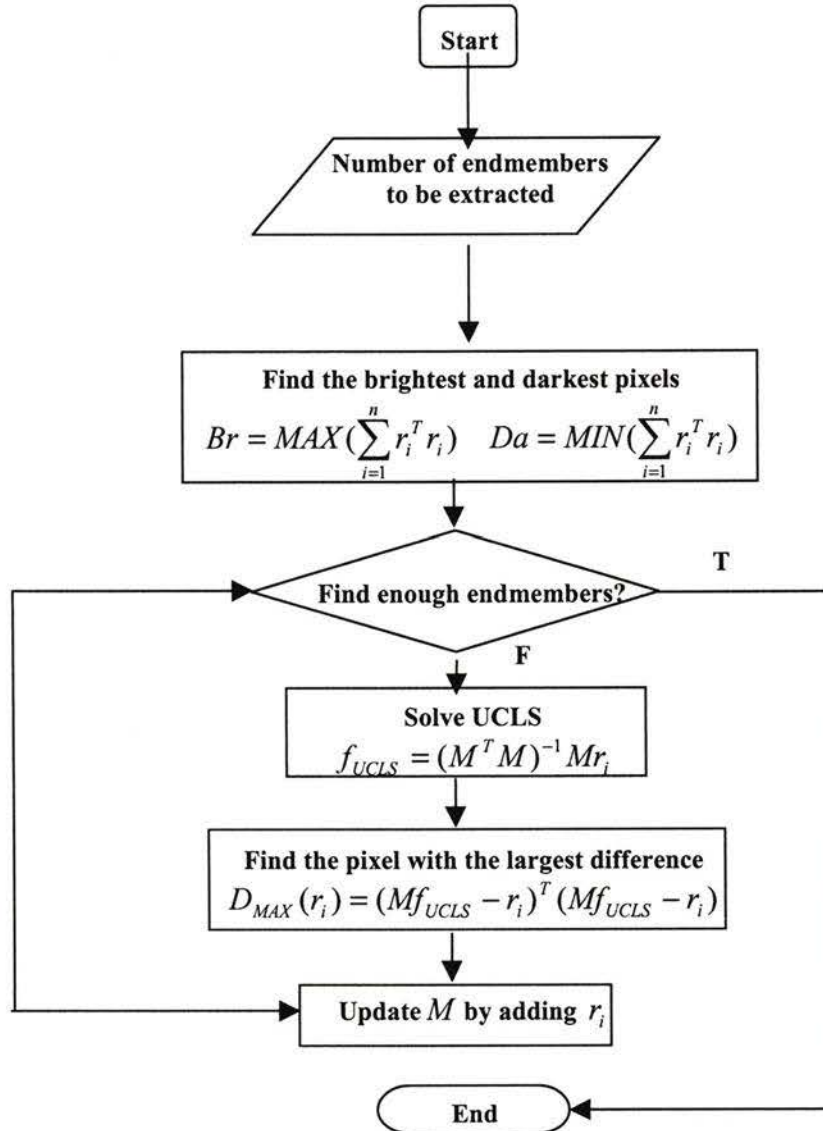


Figure 5.1 Flowchart of the Endmember Extraction Algorithm

$s \times n$ subtractions, which can be simplified as an $O(n^2)$ problem. Summing up, the cost of endmember extraction is $O(n^3)$.

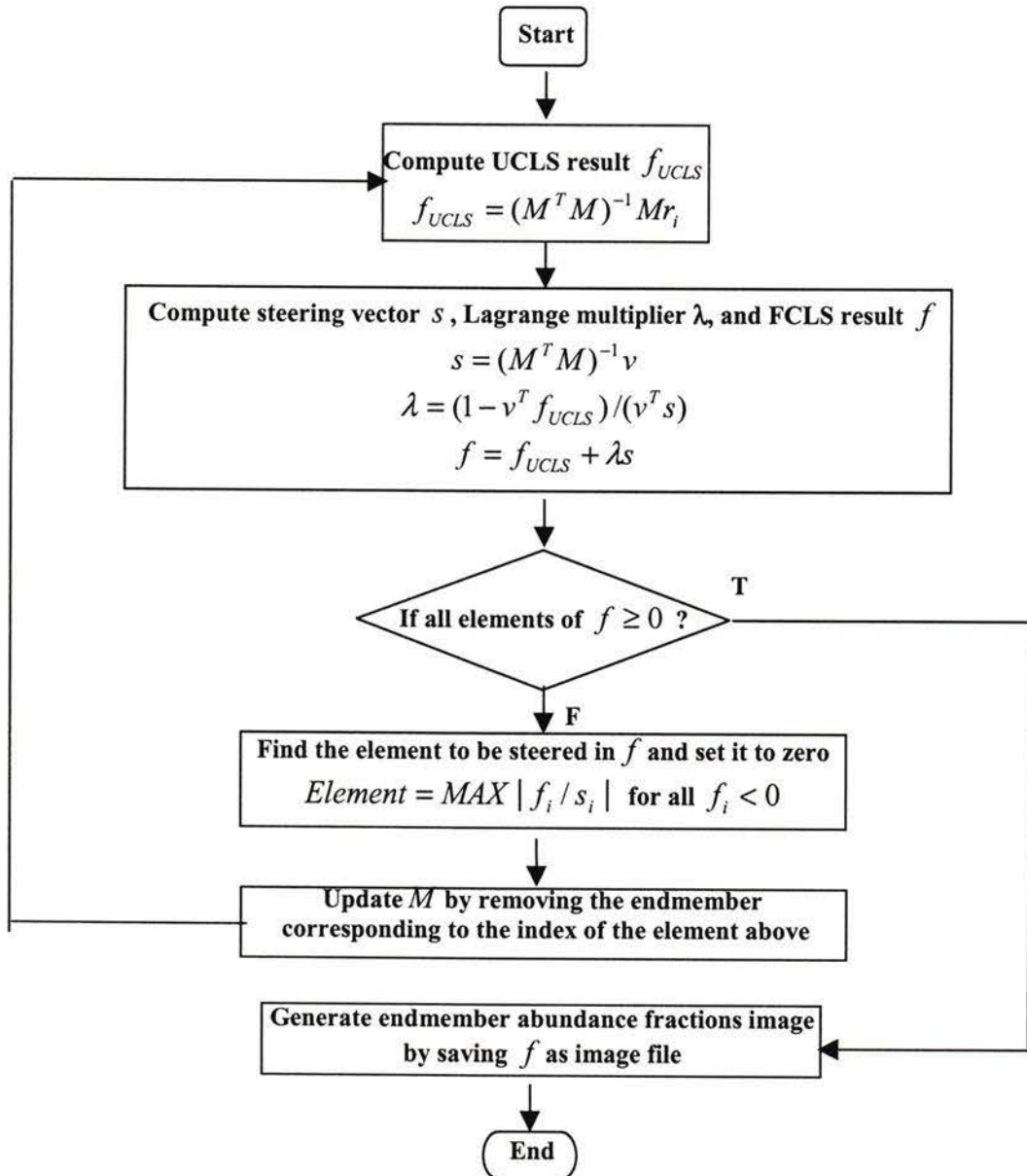


Figure 5.2 Flowchart of Fully Constrained Least Squares Spectral Unmixing Algorithm

Once the endmembers are extracted from the image, we proceed to the endmember unmixing by implementing FCLS, which includes obtaining the UCLS result, computing the Lagrange multiplier $\hat{\lambda}$, generating the steering vector s , searching for the estimated fraction to be steered, and updating the endmember spectral matrix, as discussed in Section 5.2. The algorithm is detailed in Figure 5.2.

As proved in the endmember extraction, the most expensive part of FCLS is to calculate UCLS repeatedly, which is a $O(p \times n^3)$ problem. Here p represents the number of endmembers. In normal conditions, $p \ll n$. Therefore, the problem is still considered to be of $O(n^3)$. For the worst case, every pixel in the image is unique, and then each pixel is an endmember. The cost for FCLS becomes $O(n^4)$ for $p = n$.

Chapter 6

Validation of Spectral Unmixing Results

Two linear spectral unmixing algorithms have been introduced in Chapter 4 and 5 respectively, which are derived on the basis of the localized constrained energy minimization (LCEM) and the fully constrained least squares estimation (FCLS). Here we call them LCEM spectral unmixing algorithm (LCEM_SUA) and FCLS spectral unmixing algorithm (FCLS_SUA). Because the LCEM_SUA requires the target endmember spectrum as *a priori*, it is appropriate for target detection. The FCLS_SUA does not have this restriction. It has applications for the resource pixel extraction and estimation. In this chapter these two algorithms are tested with both simulated and real hyperspectral data, which include Hyperion level 1b1 and AVIRIS data. Let us start with a brief introduction of our test site and field data acquisition.

6.1 Test Site and Field Data Acquisition

The main test site is the Greater Victoria Watershed (GVWD), which is located on Vancouver Island, BC. GVWD is a rectangular area of 15 km by 23 km (Fig. 6.1). The average elevation of GVWD is about 400 meters above sea level, with slopes as great as 45 degrees for some of the plots. Over 90 percent of the trees found in this test site are Douglas-fir. Except for the younger stands, the old growth forest is largely unmanaged. We have 54 plots inside the test site and most of them are from the unmanaged areas.

The GVWD test site contains some of the oldest stands of Douglas-fir in the southern half of Vancouver Island [17].

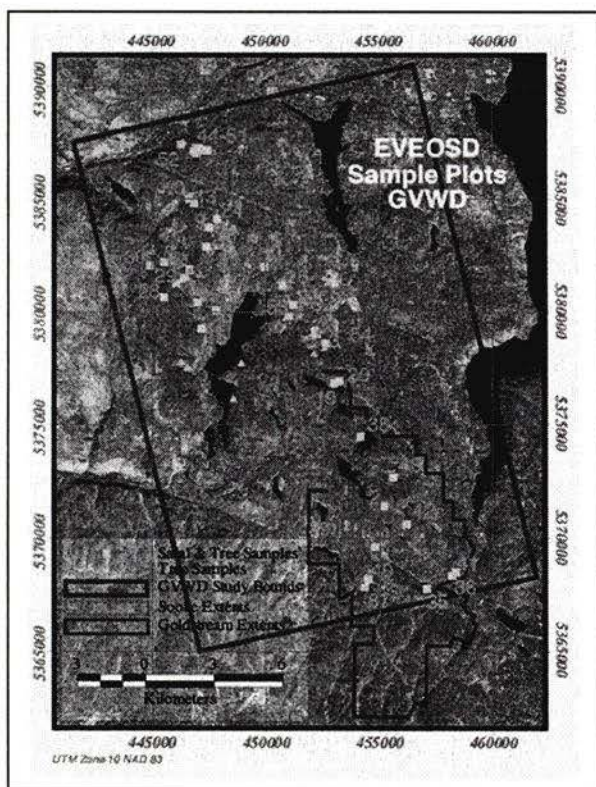


Figure. 6.1 Test Site (left) and Field Data Acquisition (right)

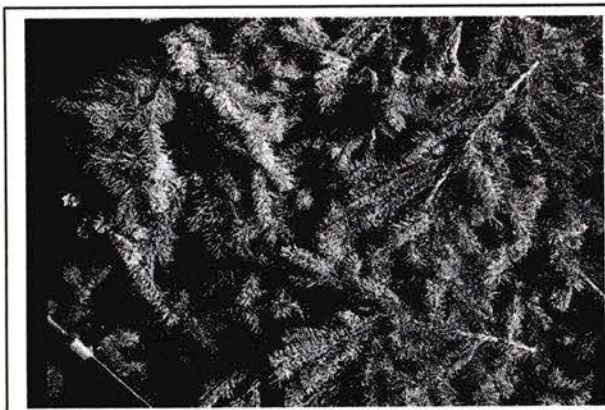
In order to get simultaneous measurements, the field campaign took place on August 10 and September 10 of 2001 during the AVIRIS and Hyperion over flights. We used the ASD field spectrometer to collect the spectra of several different targets, including treetop foliage, ground cover vegetation (mostly salal and grass), soil, shade, and water. The ASD field spectrometer has 2-nm spectral resolution with 1 nm sampling. So the collected spectra can be used to simulate the data acquired by AVIRIS and Hyperion, which have approximately 10-nm spectral resolution. While the spectra were collected, the differential Trimble GPS receiver was employed to record exactly where and when the spectra were collected. At the same time, we also took photos of the targets we

measured. All field data were placed into an Access database at PFC. These field data are crucial for the AVIRIS and Hyperion data calibration and correction.

6.2 Validation of the Results from Localized Constrained Energy Minimization Spectral Unmixing Algorithm

6.2.1 Validation with Simulated Hyperspectral Data

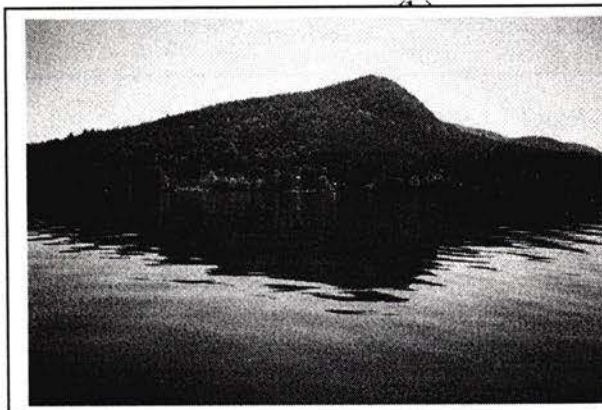
To evaluate the accuracy of the LCEM_SUA, we use simulated hyperspectral data, because the composition of each endmember spectrum can be fully controlled in the simulation process. We use five endmember spectra to generate seven hundred pixels, which are arranged in one hundred and forty columns and five rows. The pictures of the five endmember materials, Douglas-fir, grass, water, salal, and soil are given in Figure 6.2 and their spectral profiles are shown in Figure 6.3. The first row pixels are generated for the Douglas-fir detection purpose, where column-20 pixel contains 5% of the Douglas-fir spectrum, column-40 10%, column-60 20%, column-80 40%, column-100 60%, column-120 80%, and column-140 100%. Other pixels in the first row do not contain any Douglas-fir spectrum. Each of them has the same ingredient of 25% grass, water, salal, and soil. The second, third, fourth, and fifth rows are built in the same way for the detection of grass, water, salal, and soil respectively. To make them more similar to the real hyperspectral data, white Gaussian noise is added to each simulated mixed pixel, and the signal-to-noise ratio is controlled at 30:1. Examples of the simulated mixed pixel spectra with noise are given in Figure 6.4.



(a)



(b)



(c)



(d)



(e)

Figure 6.2. Endmember material ((a) Douglas-fir, (b) Grass, (c) Water, (d) Salal, and (e) Soil

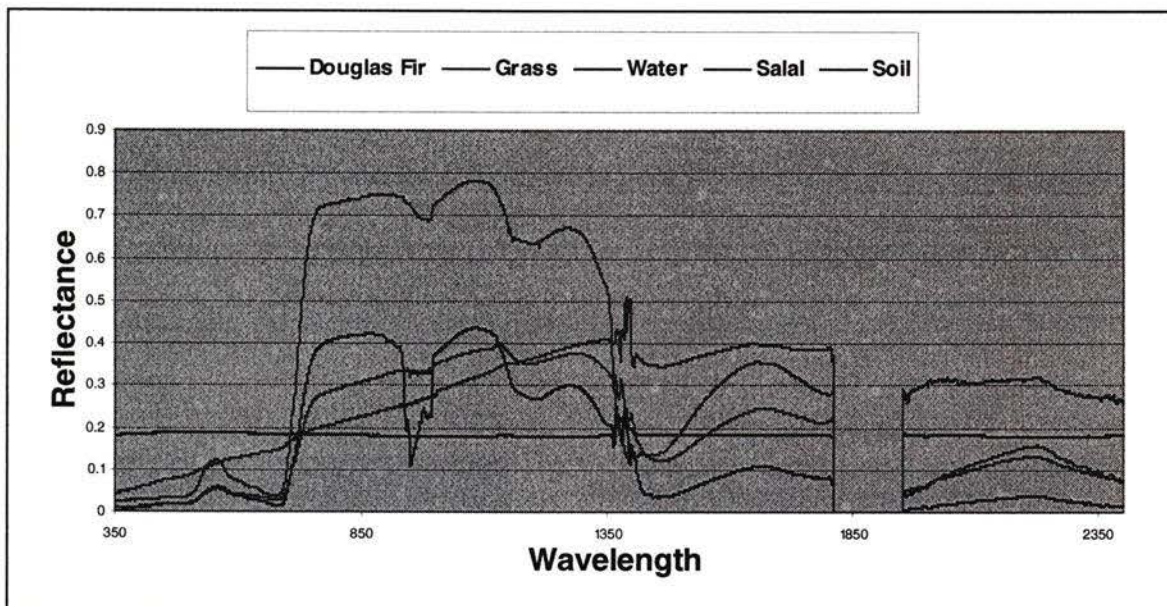


Figure 6.3 Target Spectra in Reflectance

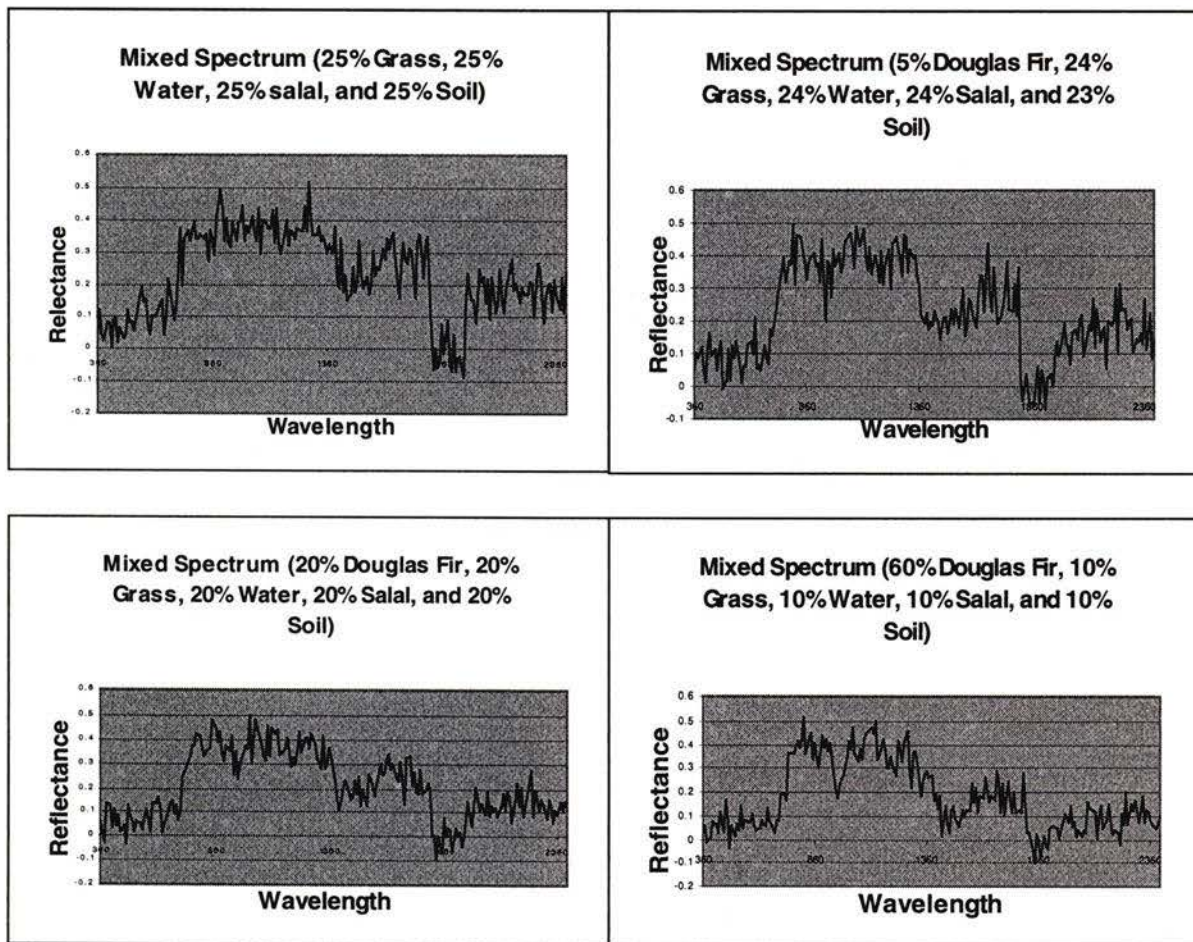


Figure 6.4 Examples of the Simulated Hyperspectral Data for Testing Constrained Energy Minimization Spectral Unmixing Algorithm

The simulated hyperspectral data are first used to validate the CEM based spectral unmixing algorithm (CEM_SUA). We use the first row data (pixel 1 – 140) for Douglas fir spectrum unmixing, the second row (pixel 141 – 280) for grass, the third row (pixel 281 – 420) for water, the fourth row (pixel 421 – 560) for Salal, and the fifth row (pixel 561 – 700) for soil, respectively. The CEM_SUA results are shown in Figure 6.5.

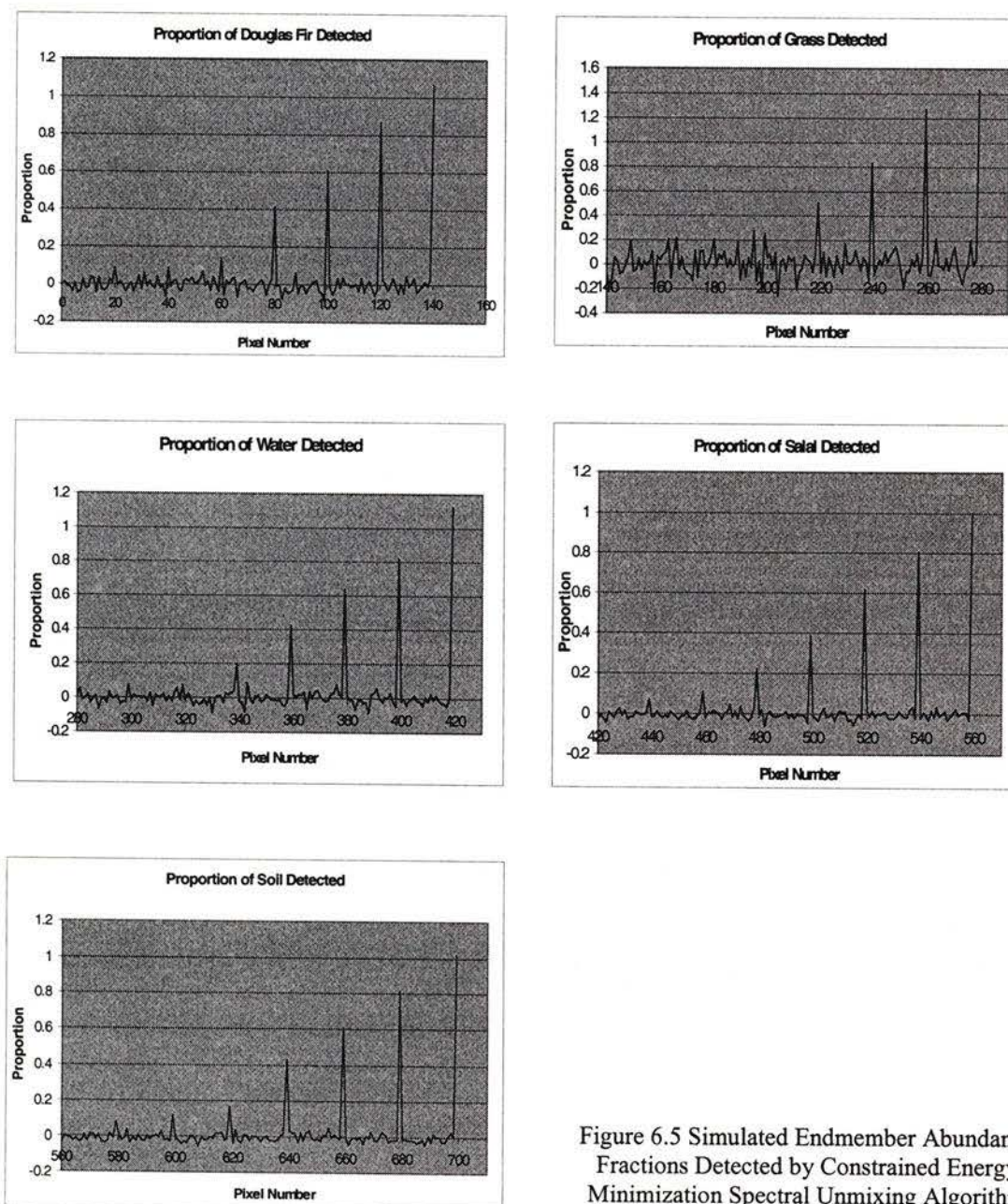


Figure 6.5 Simulated Endmember Abundance Fractions Detected by Constrained Energy Minimization Spectral Unmixing Algorithm

Table 6.1 Comparison between Real and Computed Results by Constrained Energy Minimization Spectral Unmixing Algorithm

Real fractions (%)	0	5	10	20	40	60	80	100
Computed fractions of Douglas fir (%)	1	8	9	21	41	60	86	101
Computed fractions of grass (%)	-7	4	20	25	51	83	92	123
Computed fractions of water (%)	0	7	7	16	42	64	82	112
Computed fractions of salal (%)	-3	7	11	22	39	62	80	100
Computed fractions of soil (%)	-3	8	12	17	43	61	82	102
Mean error (%)	2.8	2.2	3.4	3.0	3.6	4.0	4.4	9.5

The results show that CEM_SUA works fine for most cases. It gives the correct or close to correct target abundance proportions. However, there is room for improvement. We notice that when the proportion of some target endmember spectra are below 20%, CEM has difficulty to detect them. The endmember spectra are buried by the background spectra and noise. CEM also tends to over estimate the abundance proportions of the dominated endmembers and under estimate the low abundance endmembers.

To improve the CEM_SUA results, we use LCEM_SUA to unmix the same data set. As introduced in Chapter 4, LCEM_SUA uses local covariance matrices instead of the single global covariance matrix in the CEM_SUA. So we first separate each row of data into seven groups, 20 pixels each, then compute the covariance matrices for each group, perform spectral unmixing, and normalize the results. The LCEM_SUA results are shown in Figure 6.6. Compared with CEM_SUA results, it is demonstrated that the LCEM_SUA can effectively suppress the background spectra and noise, detect small targets, and produce more accurate target endmember proportion results. The mean error is reduced from 4.1% in CEM to 1.6% in LCEM. LCEM can detect the endmembers with 10% abundance.

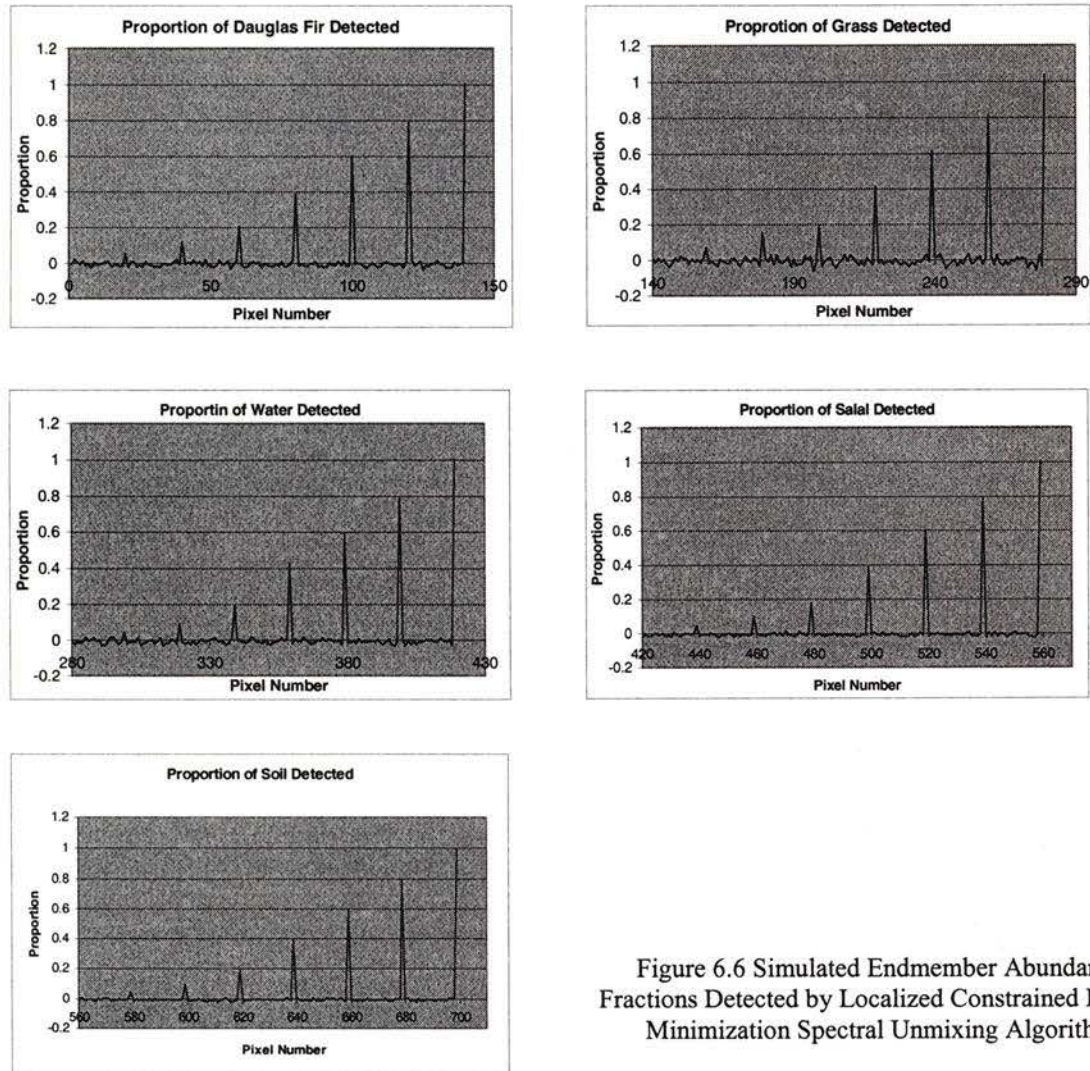


Figure 6.6 Simulated Endmember Abundance Fractions Detected by Localized Constrained Energy Minimization Spectral Unmixing Algorithm

Table 6.2 Comparison between Real and Computed Results by Localized Constrained Energy Minimization Spectral Unmixing Algorithm

Real fractions (%)	0	5	10	20	40	60	80	100
Computed fractions of Douglas fir (%)	-1	5	12	21	38	60	79	100
Computed fractions of grass (%)	2	7	15	19	42	68	82	104
Computed fractions of water (%)	0	4	9	17	43	64	81	100
Computed fractions of salal (%)	-3	5	10	18	39	59	84	101
Computed fractions of soil (%)	-1	4	10	19	40	62	79	100
Mean error (%)	1.4	0.8	1.6	1.6	1.6	3.0	1.8	1.0

6.2.2 Validation with Hyperion Data

The Hyperion data (Figure 2.3) were acquired over GVWD on Sept. 10, 2001 and have been processed to level 1b1 by TRW. Before they are used for the spectral unmixing, two more processing steps are required, which are the striping and smiling corrections [20]. See Appendices 2 and 3 for details. Because it has been demonstrated in Section 6.2.1 that LCEM_SUA has better performance than CEM_SUA, from now on we only consider LCEM_SUA.

LCEM_SUA requires target spectra *in priori*, which are usually obtained with a field spectrometer (Figure 6.2) or from a spectral library. Before starting to unmix the Hyperion data, we need to convert the data into reflectance by running atmospheric correction software, such as FLAASH or ACORN [14]. Unfortunately these programs do not work very well with the Hyperion data that have lower signal-to-noise ratio. To solve the problem of using field reflectance data directly, we extract target spectra directly from the Hyperion image being processed, and then plug them into the LCEM_SUA without requiring the atmospheric correction. Four target spectra are extracted from the image, which correspond to forest, grass, water, and soil (Figure 6.7). The unmixing results are expressed in target abundance fraction images, which are shown in Figure 6.8, in which the brighter pixels represent the higher concentration or fraction of the corresponding target endmembers.

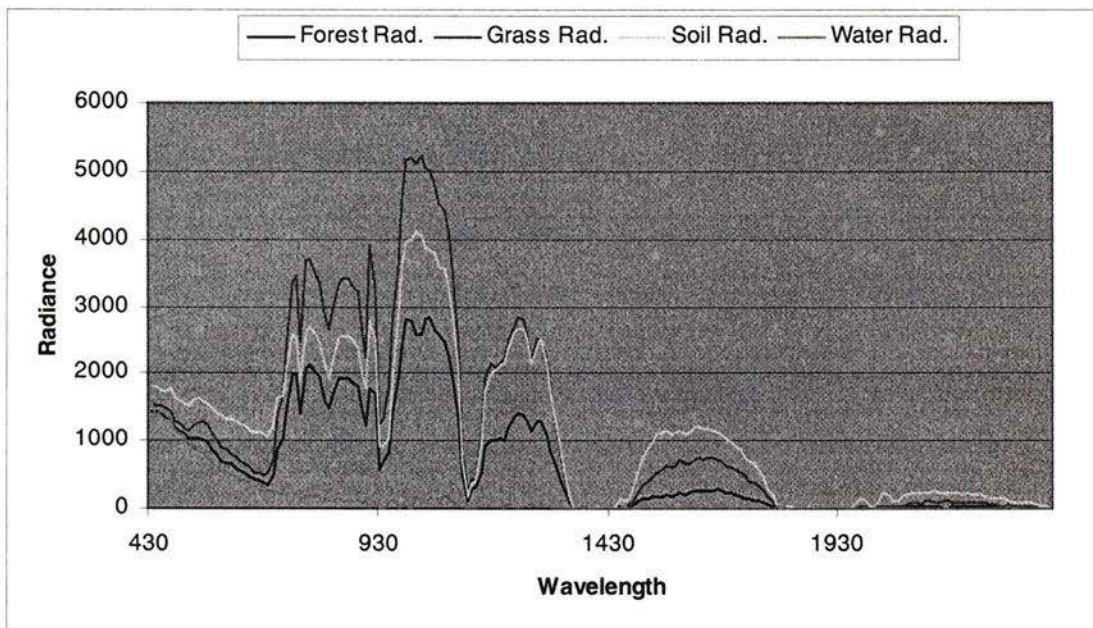


Figure 6.7 Hyperion Endmember Spectra in Radiance Extracted from Image

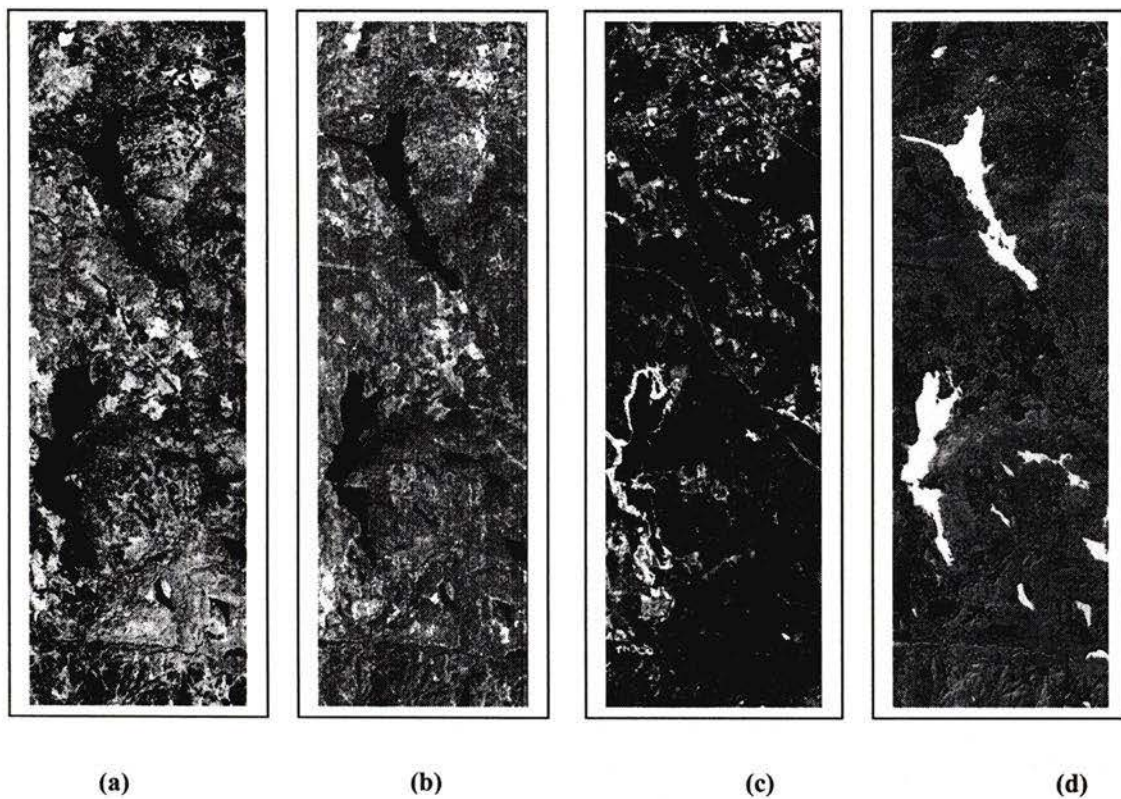


Figure 6.8 Hyperion Endmember Fraction Images Created by Localized Constrained Energy Minimization Spectral Unmixing Algorithm ((a) forest, (b) grass, (c) soil, and (d) water)

To evaluate the LCEM unmixing accuracy with Hyperion data, we first convert the endmember fractions (Figure 6.8) into bitmap images by setting a threshold, which is 0.60. That is, if a fraction value is larger than 0.60, the corresponding pixel value is set to 1; otherwise it is set to 0. Then Spectral Angle Mapper (SAM) supervised classifier, provided in ENVI, is employed to classify the Hyperion image with endmember spectra shown in Figure 6.7. The classification results are shown in Figure 6.9. The bitmap images and the corresponding SAM classification results are compared. Their differences are used as a reference of the unmixing accuracy, which is shown in Table 6.3. The comparison reveals that the results obtained by these two approaches are fairly close. The largest difference happens on forest, which is 2.0% of total image pixels.

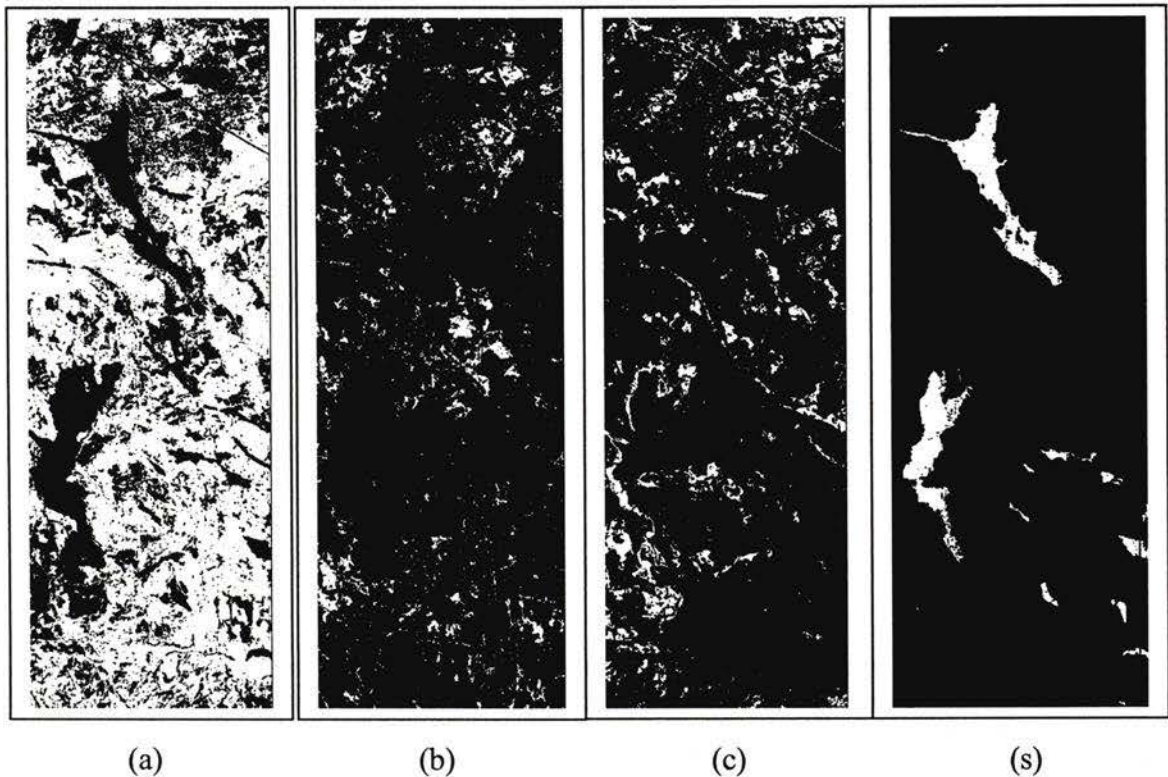


Figure 6.9 Classification Results by Spectral Angle Mapper ((a) forest, (b) grass, (c) soil, and (d) water)

Table 6.3 Result Comparison between Localized Constrained Energy Minimization Spectral Unmixing and Spectral Angle Mapper Classification with Hyperion Data

	Forest	Grass	Soil	Water
Number of Pixels marked by SAM	125948	17755	22358	10609
Number of Pixels Marked by LCEM_SUA	130051	18826	23944	11572
Number Difference/Total Image pixels	2.0%	0.5%	0.8%	0.5%

6.2.3 Validation with AVIRIS Data

The AVIRIS data (Figure 2.2) were collected over GVWD on Aug. 10, 2001. Compared with the Hyperion data, the AVIRIS data are of better quality – higher SNR and better spatial resolution (20 m). General speaking, AVIRIS data can be atmospherically corrected by ACORN or FLAASH, though they still have problems to correct water spectrum and may generate false spectra. Before unmixing the AVIRIS data with LCEM_SUA, we use FLAASH for the atmospheric correction and generate an AVIRIS reflectance image. Then the same endmember spectra as shown in Figure 6.2 are employed as target endmembers, for which the water spectrum is not included. The spectral unmixing results by LCEM_SUA are organized in Figure 6.10. To evaluate the unmixing accuracy of AVIRIS data, the same strategy is followed as we did to the Hyperion data. The difference between SAM classification and LCEM spectral unmixing is organized in Table 6.4.

Table 6.4 Result Comparison between Localized Constrained Energy Minimization Spectral Unmixing and Spectral Angle Mapper Classification with AVIRIS Data

	Forest	Grass	Soil	Salal
Number of Pixels marked by SAM	492953	69709	87768	41646
Number of Pixels Marked by LCEM_SUA	409150	73891	93911	38314
Number Difference/Total Image pixels	1.7%	0.6%	0.7%	0.8%

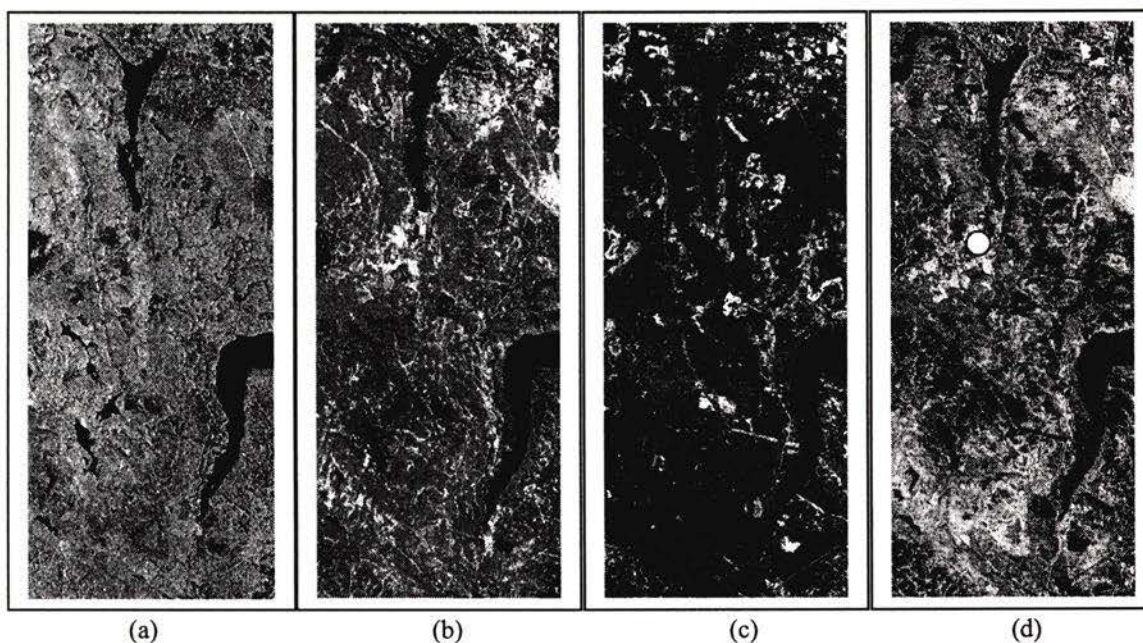


Figure 6.10 AVIRIS Endmember Fraction Images Created by Localized Constrained Energy Minimization Spectral Unmixing Algorithm ((a) forest, (b) grass, (c) soil, and (d) salal)

It is our goal to separate and recognize vegetation at the sub-pixel level from remote sensing images, which cannot be achieved by visual inspection or pixel based classification. For example, salal is bush-like small vegetation, which is very bright in the near infrared (Figure 6.2). In GVWD, salal usually grows under tall trees, like Douglas fir, which is illuminated by the sunlight through the gaps in the forest canopy. As a matter of fact, many forest pixels have salal content in them. Determining the salal abundance fractions in forest pixels and finding the most salal concentration area in GVWD is a subject of great interest as the salal chemistry differs from that of the Douglas-fir. Such information is very useful for other forest related studies, such as forest carbon stock estimations. The salal abundance fraction image ((d) of Figure 6.8) generated by LCEM_SUA provides this information (the red circle encloses the area with the highest salal concentration).

6.3 Validation of Results from Fully Constrained Least Squares Spectral Unmixing Algorithm

6.3.1 Validation with Simulated Hyperspectral Data

Unlike the LCEM_SUA method, the FCLS_SUA method extracts endmember spectra from the image being processed. To validate FCLS_SUA, we use the same field spectral data as we used for the LCEM_SUA validation to generate the simulated hyperspectral data. Five rows of data, one hundred and twenty pixels each, are generated. The first row of data is for salal unmixing purpose, which has the following composition.

Table 6.5 Compositions of Simulated Pixels

Pixel 1	100% Salal	Pixel 40	60% Salal. 40% others
Pixel 2	100% Douglas Fir	Pixel 60	40% Salal. 60% others
Pixel 3	100% Grass	Pixel 80	20% Salal. 80% others
Pixel 4	100% Water	Pixel 100	10% Salal. 90% others
Pixel 5	100% Soil	Pixel 120	5% Salal. 95% others
Pixel 20	80% Salal. 20% others	Other Pixels	20% each

The remaining rows are constructed in the same way for other endmember unmixing as the first row. The white Gaussian noise with zero mean is created and added to the above data with a signal-to-noise-ratio of 40 to 1, for the FCLS_SUA can not handle the data with a SNR lower than this threshold. Two examples of the simulated mixed spectra are given in Figure 6.11.

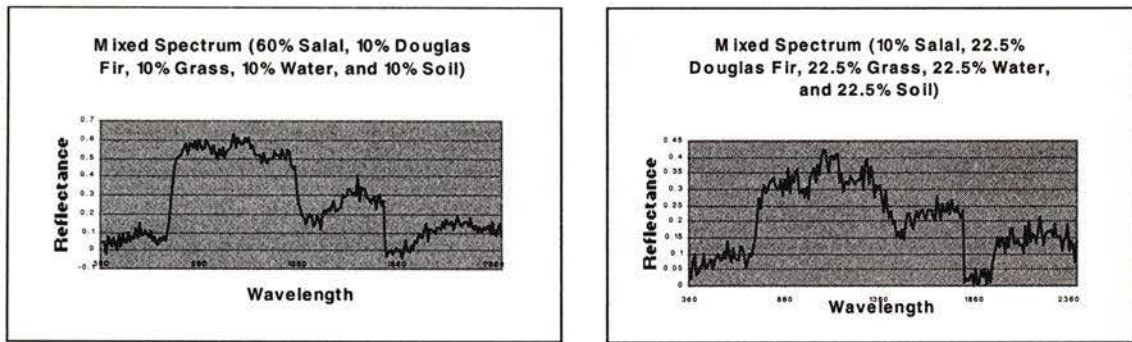


Figure 6.11 Examples of Simulated Hyperspectral Data for Testing Fully Constrained Least Squares Spectral Unmixing Algorithm

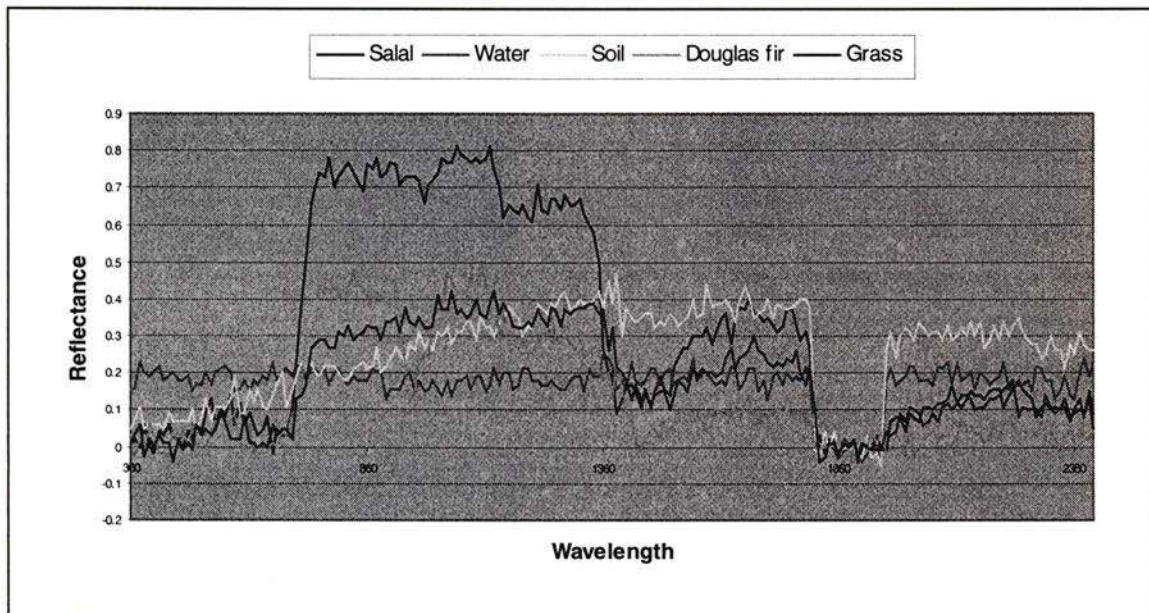


Figure 6.12 Simulated Endmember Spectra Detected by Fully Constrained Least Squares Spectral Unmixing Algorithm

Once the simulated data are created, the FCLS_SUA is first used to extract the endmember spectra, which are then used for spectral unmixing. It should be noted that the extracted spectra are actually the combination of the pure spectra and the added white Gaussian noise (Figure 6.11), which is different from but more realistic than the LCEM_SUA, where we used pure spectra as endmembers. The experiment reveals that the unmixing result is corrupted with the lower signal-to-noise-ratio. When the SNR is

below 40, some mixed spectra are erroneously selected as endmember spectra, for the noisy data confuses the endmember extraction algorithm, which is based on the unconstrained least squares estimation. Fortunately the SNR of the real hyperspectral data is well above this threshold (above 100 for Hyperion and 1000 for AVIRIS). The FCLS_SUA unmixing results are shown in Figure 6.13 and Table 6.6, which are more optimal than that of the LCEM_SUA. All endmember fractions are no longer negative.

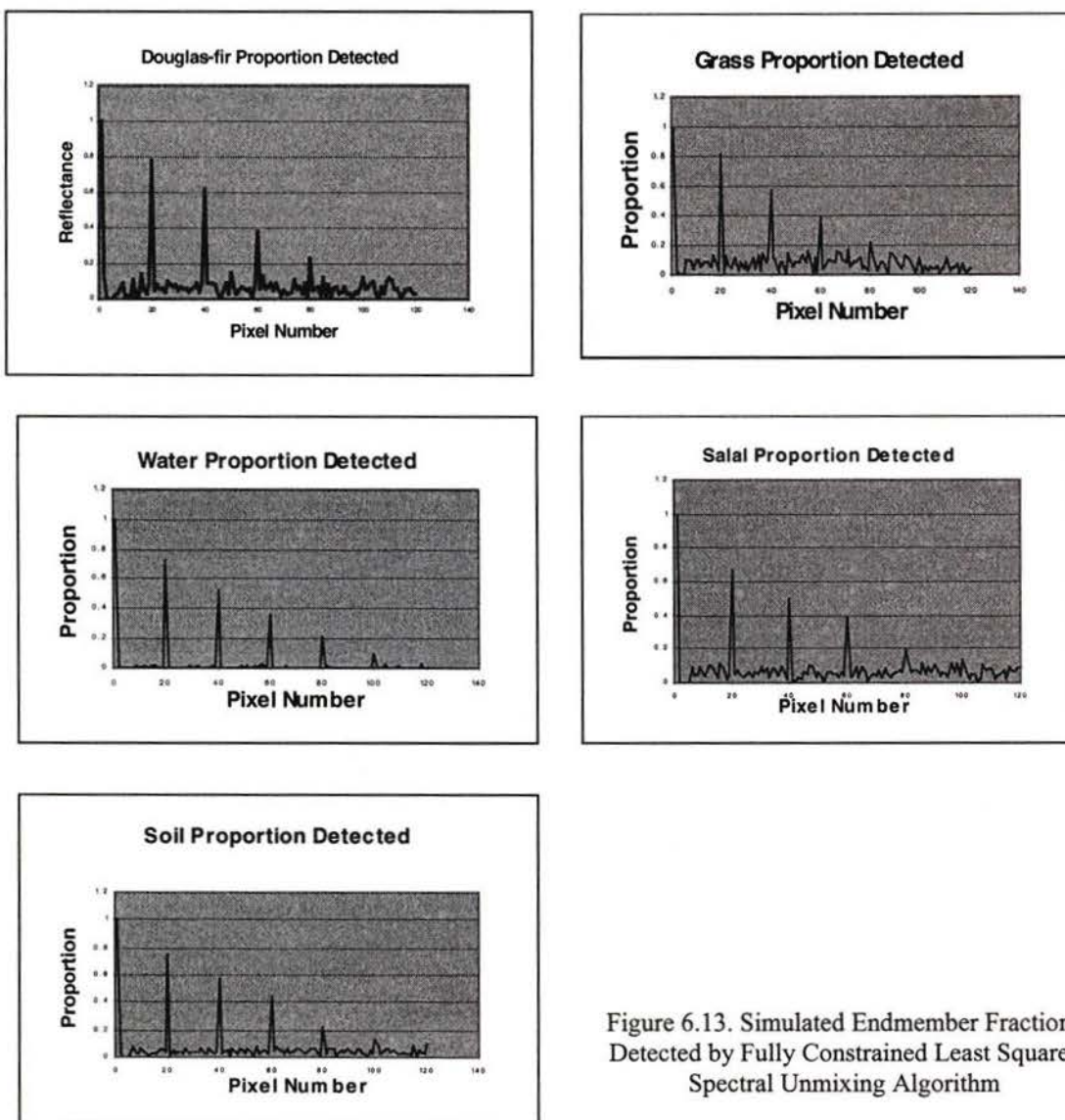


Figure 6.13. Simulated Endmember Fractions Detected by Fully Constrained Least Squares Spectral Unmixing Algorithm

Table 6.6 Comparison between Real and Computed Results by Fully Constrained Least Squares Spectral Unmixing Algorithm

Real fractions (%)	0	5	10	20	40	60	80	100
Computed fractions of Douglas fir (%)	2	6	12	22	41	60	79	100
Computed fractions of grass (%)	1	7	12	21	42	58	82	100
Computed fractions of water (%)	2	5	11	21	37	57	78	100
Computed fractions of salal (%)	2	3	10	22	41	55	74	100
Computed fractions of soil (%)	3	8	13	24	44	60	79	100
Mean error (%)	2.0	1.6	1.6	2.0	2.2	2.0	2.4	0.0

6.3.2 Validation with Hyperion Data

As for the LCEM_SUA validation, we used the same radiance Hyperion data to validate FCLS_SUA. Eight unique spectra are extracted as endmember candidates (Fig 6.14).

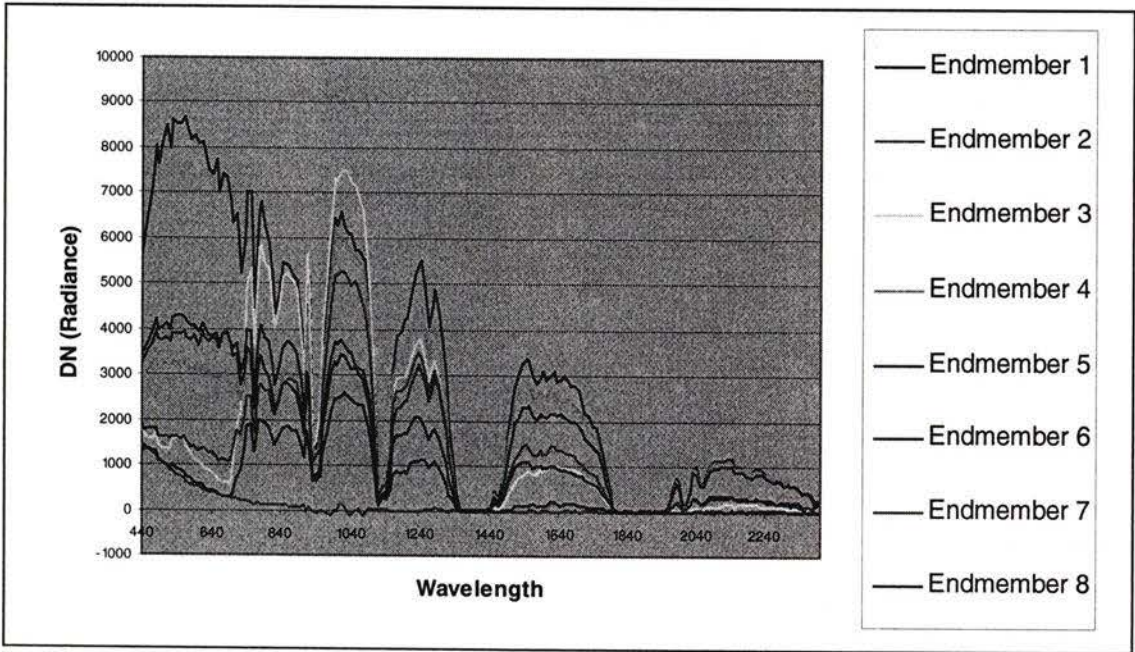


Figure 6.14 Hyperion Endmember Spectra Detected by Fully Constrained Least Squares Spectral Unmixing Algorithm

Endmember 1 corresponds to the brightest pixel in the image, which is located in a soil area. From its location and spectral profile, it looks like a kind of soil or rock.

Endmember 2 corresponds to the darkest pixel in the image, which is water. Endmember 3 has vegetation feature and is very bright in the near infrared, which looks like salal or some kind of grass. Endmembers 4, 5, 6, and 7 are all found in soil areas with different degrees of grass or vegetation cover. Endmember 8 is forest. Selecting endmembers 1, 2, 4, and 8 as target spectra representing soil, water, grass, and forest, respectively, we obtain the spectral unmixing results by FCLS_SUA (Figure 6.15) and compare the unmixing results with SAM classification in Table 6.7, which are consistent with LCEM results.

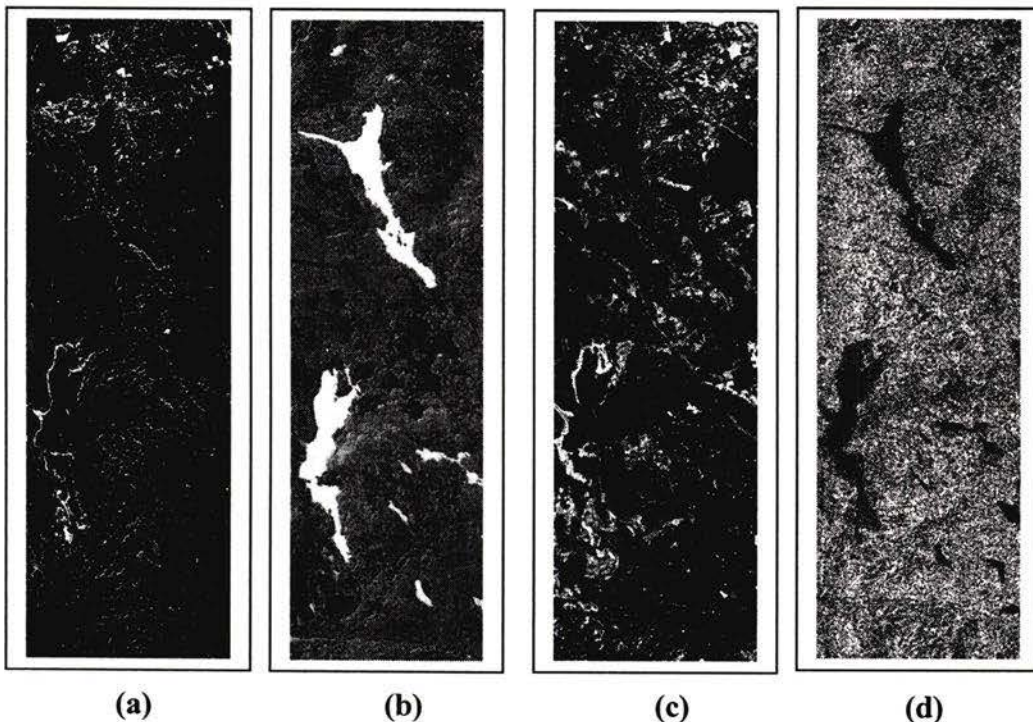


Figure 6.15 Hyperion Endmember Fraction Images Created by Fully Constrained Least Squares Spectral Unmixing Algorithm ((a) Endmember 1(soil), (b) Endmember 2 (water), (c) Endmember 4 (grass), (d) Endmember 8 (forest)

Table 6.7 Result Comparison between Fully Constrained Least Squares Spectral Unmixing and Spectral Angle Mapper Classification with Hyperion Data

	Soil	Water	Grass	Forest
Number of Pixels marked by SAM	22358	10609	17755	125948
Number of Pixels Marked by FCLS_SUA	20512	12044	15499	129844
Number Difference/Total Image pixels	0.9%	0.7%	1.1%	1.9%

6.3.3 Validation with AVIRIS Data

Before using AVIRIS image for the FCLS_SUA validation, we first correct it into reflectance with FLAASH as we did before. Eight endmember spectra are extracted by FCLS_SUA, which are shown in Figure 6.16. The first endmember is too bright to be believed (over 100% reflectance), which looks like a false spectrum created by the atmospheric correction program. Apparently endmember 2 is water. Endmember 3 has a vegetation-like spectral profile and is pretty bright in near infrared. It is very likely to be the Salal. Endmember 4, 5, and 6 are all located in soil areas. They correspond to the soils with different vegetation recovering levels. Endmember 7 sounds like a false spectrum too. The red-edge, vegetation-like spectral profile, and its location tell that endmember 8 is forest. The endmember detected here are basically consistent with that detected from the Hyperion image.

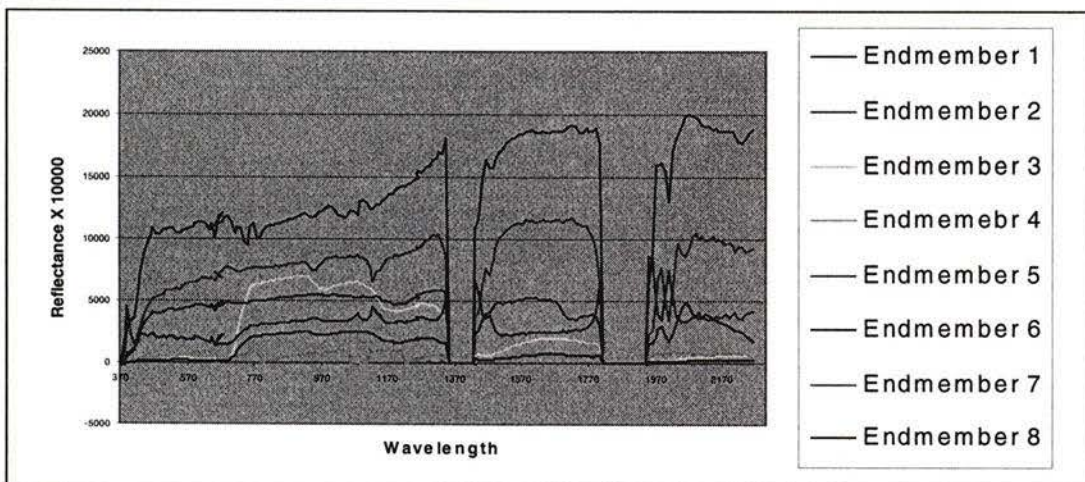


Figure 6.16 Endmember Spectra Extracted from AVIRIS Image by Fully Constrained Least Squares Spectral Unmixing Algorithm

Endmembers 2, 3, 4, and 8 are selected as targets for spectral unmixing. They are water, salal, soil, and forest. The unmixing results are given in Figure 6.17. From the salal unmixing result, the spot with the highest salal concentration (red circle area in (b) of Figure 6.17) is located, which is in the same area detected by LCEM_SUA.

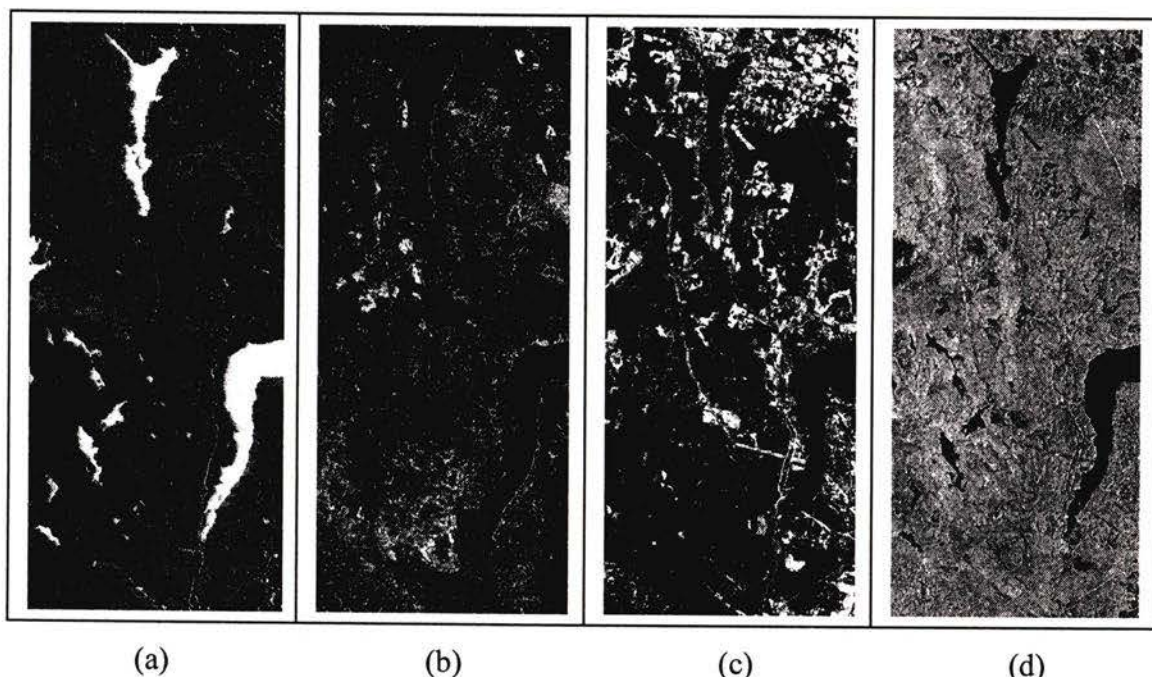


Figure 6.17 AVIRIS Endmember Fraction Images Created by Fully Constrained Least Squares Spectral Unmixing Algorithm ((a) Endmember 2 (water) (b) Endmember 3 (salal) (c) Endmember 4 (soil) and (d) Endmember 8 (forest))

Table 6.8 Result Comparison between Fully Constrained Least Squares Spectral Unmixing and Spectral Angle Mapper Classification with AVIRIS Data

	Water	Salal	Soil	Forest
Number of Pixels marked by SAM	13882	41646	87768	492953
Number of Pixels Marked by LCEM_SUA	14686	37621	80523	481683
Number Difference/Total Image pixels	0.1%	0.5%	1.2%	1.4%

Chapter 7

Hyperspectral Unmixing Software Development

Hyperspectral image unmixing has many applications in forestry, agriculture, environment, military, etc [12]. With more hyperspectral sensors being built and more data being acquired, the need for automated hyperspectral unmixing software has become apparent. In this chapter, we discuss the unmixing software development issues, which include the limitations of the current commercial hyperspectral spectral unmixing software, programming language selection, and the unmixing algorithm implementation.

7.1 Limitations of Current Commercial Spectral Unmixing Software

Hyperspectral unmixing algorithms have been studied intensively in the past decade. Only a few algorithms have been implemented into commercial remote sensing software. The most popular commercial software for hyperspectral analysis is the Environment for Visualizing Images (ENVI), which is based on convex geometry for spectral unmixing [14]. The following steps are needed for a user of ENVI to find endmembers from a given hyperspectral image:

- Apply the Minimum Noise Fraction (MNF) transformation to find the inherent data dimensionality, remove noise, and reduce data volume.
- Apply Pixel Purity Index (PPI) analysis to the MNF output to rank the image pixels based on relative purity and spectral extremity. The pixels with high PPI values most

likely correspond to the purest pixels containing a single endmember. PPI further reduces the data volume.

- The user performs n-Dimensional Visualization to find the high PPI value pixels. The user rotates the data in 3 or more dimensions and determines the number of endmembers. The spectral signatures of the endmembers are then extracted.
- The user compares the spectral signatures with the spectra in the predefined spectral library to determine what kind of material occurs on the ground corresponding to each pixel of the image.
- The user generates the endmember abundance proportion images.

It is not easy for most users to obtain their endmembers through these steps. On the one hand, they need to understand what is going on for each of the steps, which requires the understanding of the concepts of linear algebra and system optimization. On the other hand, user intervention is needed. The users have to manually locate the endmembers in a hyperspace, and extract them one by one. This is not an automatic process.

Keeping the above drawbacks in mind, we implemented our unmixing algorithms, discussed in Chapters 4 and 5 to develop our own automated, hyperspectral unmixing software. No user intervention is needed to run this program. For the users who just want results, the program can be used as a “black box”. For the advanced users who want to know how the algorithms and how the system works, they can be satisfied by reading the related documentation through the program’s on-line help and this thesis.

7.2 Programming Language

Remote sensing images can be easily stored and manipulated in 3D arrays with the first 2D representing spatial locations and the third dimension representing the spectral locations. Remote sensing data processing, such as spectral unmixing, usually requires dynamic data volume expansion and contraction. So the programming languages with dynamic binding, dynamic memory allocation, and automatic garbage collection will be helpful. Spectral unmixing involves intensive matrix manipulations, such as eigenvector analysis and singular value decomposition, which requires the programming languages to have powerful mathematical libraries. Additionally, the program language should provide some tools to facilitate graphical user interfaces.

Interactive Data Language (IDL), developed by Kodak's Research Systems Inc., is a complete computing environment for the interactive analysis and visualization of data [13]. IDL integrates a powerful, array-oriented language with many mathematical analysis and graphical display tools. The important features of IDL include:

- IDL is a complete, structured language that can be used both interactively and to create sophisticated functions, procedures, and applications.
- Operators and library functions work on entire arrays (without using loops), simplifying interactive analysis and reducing programming time.
- Immediate compilation and execution of IDL commands provides instant feedback and hands-on interaction.

- Rapid 2D plotting, multi-dimensional plotting, volume visualization, image display, and animation make it possible to observe the computation results immediately.
- IDL widgets can be used to quickly create multi-platform graphical user interfaces for application programs.
- IDL supports dynamic binding without type checking, easy variable declaration and definition, and variable types can be modified during runtime.
- IDL programs run the same across all supported platforms (UNIX, Microsoft Windows, and Macintosh systems) with little or no modification.

The above features make IDL the ideal programming tool to process remote sensing data. Programming in IDL is a timesaving and effective alternative to programming with other languages. Actually ENVI is implemented in IDL. Software implemented in IDL integrates easily with other ENVI functionality. For these reasons, IDL was chosen to implement our spectral unmixing algorithms.

7.3 Software Development

IDL is an event-driven procedural language. A common IDL program usually has at least two modules – a widget definition model and an event handler module. The widget definition model is responsible for creating and defining widgets, the graphical elements that the user interacts with to convey information into or out of a program. The common IDL widgets include buttons, slider bars, and fields. By combining the widgets, we generate the graphical user interface (GUI) of our spectral unmixing program. The event-

handler module is a program module, which processes or responds to widget events, the triggers or user interactions that drive the widget program. The spectral unmixing algorithms are implemented in event-handler modules. The whole program consists of 5 function blocks as follows:

- User Interface

The user interface is programmed with the IDL widget toolkit. Each of these widgets is first created in the widget definition module, and then linked to the event handler module to process or responds to widget events. The user interface is graphical, interactive, and event-driven (Figure 7.1 and 7.2).

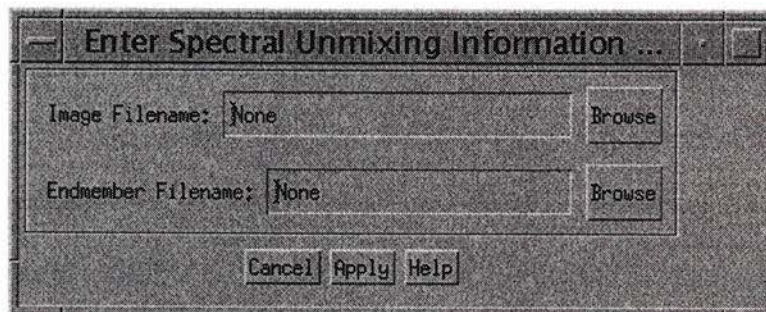


Figure 7.1 Image and Endmember Spectrum Input GUI

- User Input

The program takes user input in standard ENVI format for images, such as band sequential (BSQ), band interleaved by pixel (BIP), and band interleaved by line (BIL), and plain text format for spectral data. It is also able to parse the image header file to extract the information for image display and follow-on image processing (Figure 7.2).

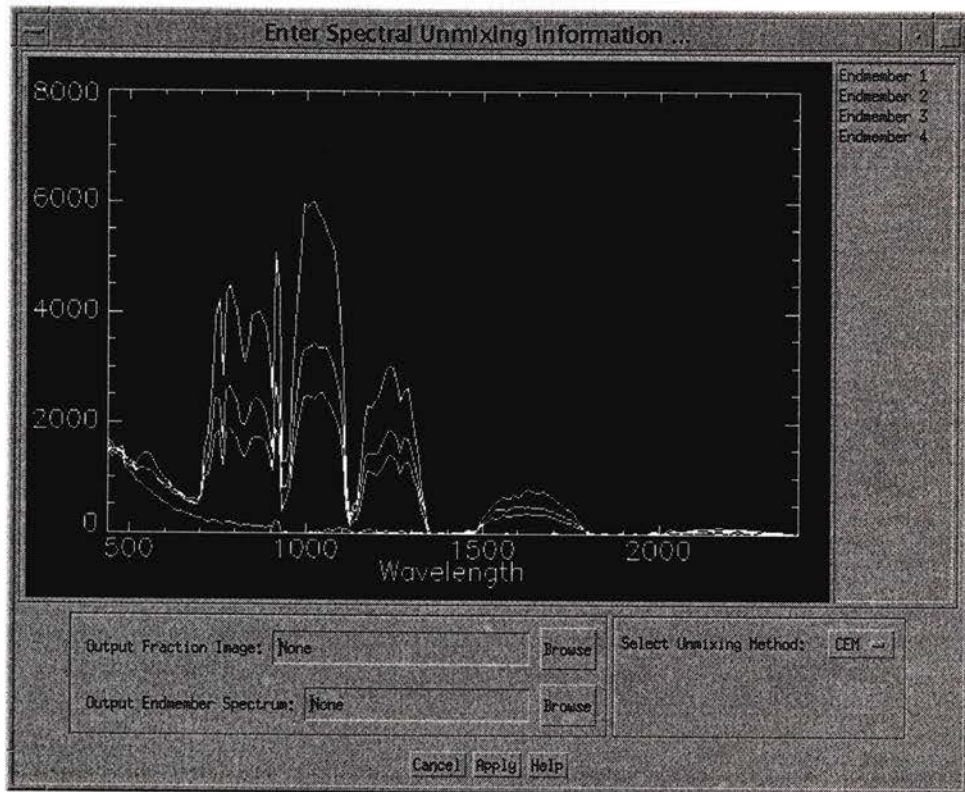


Figure 7.2 Endmember Display and Unmixing Method Selection GUI

- **Data Processing**

Endmember extraction, LCEM and FCLS spectral unmixing are implemented in the data processing block, which is the most computing intensive part of the program.

- **Results Output**

The output of the program includes the extracted endmember spectra and endmember abundance fraction images. The extracted endmember spectra are also saved in text format. The endmember abundance fraction images are saved in standard ENVI format.

- **On-line Help**

The program provides the functionality of on-line help. When the question mark button is pressed, the on-line help is activated. Any right click on widgets afterwards will generate a help window, and the related help information will be displayed.

The following block diagram (Fig. 7.3) gives the main steps involved in the spectral unmixing program.

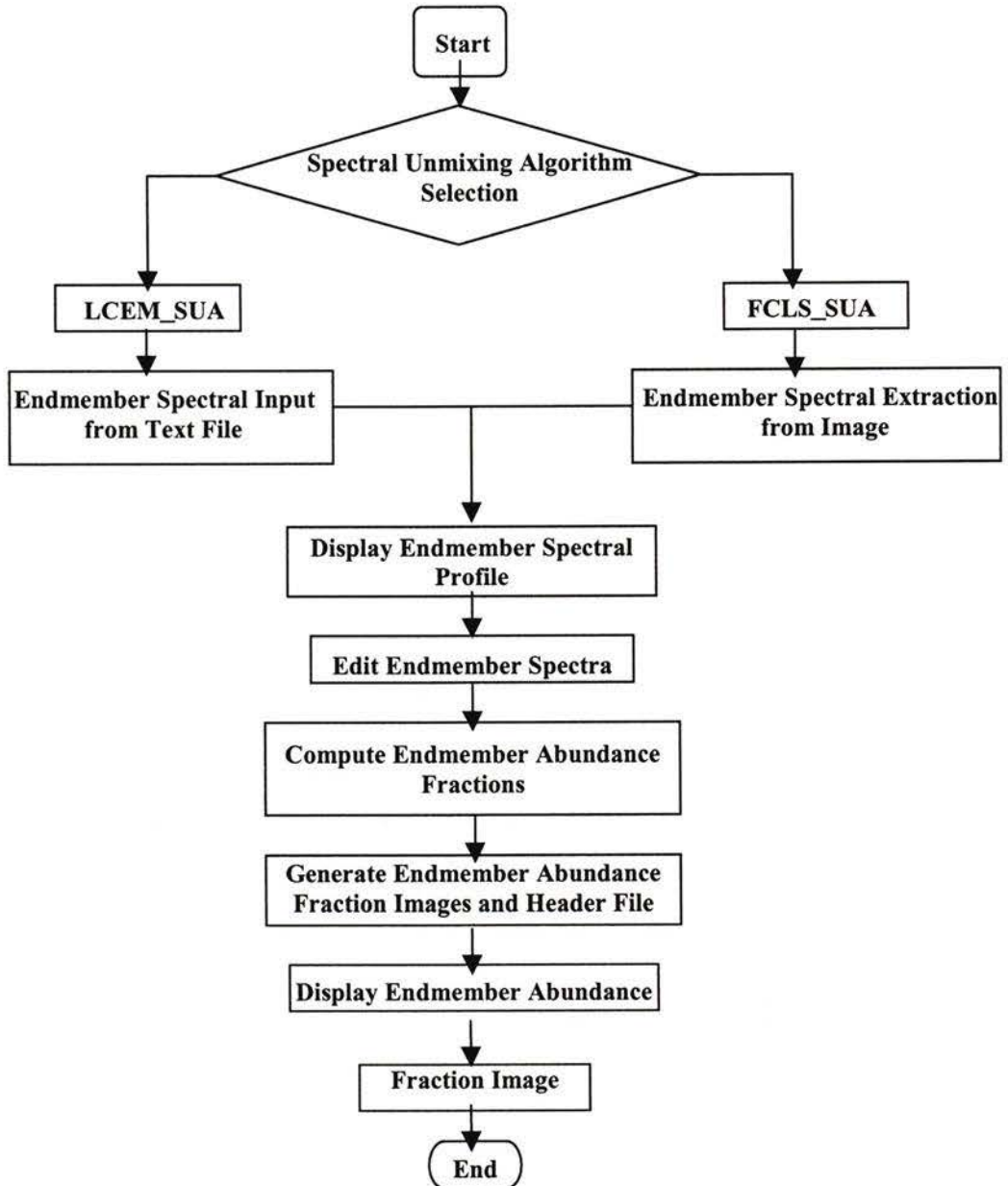


Figure 7.3 Program Block Diagram

The spectral unmixing program developed in this thesis is named as “AftAutoSpecUnmix”, which means that this is an automatic spectral unmixing program developed in the Advanced Forest Technologies Laboratory (AFT) of Pacific Forestry Centre. Because “AftAutoSpecUnmix” is programmed in IDL and uses some ENVI library functions, IDL and ENVI environments are required. There are two ways to run this program, either through command line or ENVI user interface. For the command line case, users need to run ENVI first, and then type in “AftAutoSpecUnmix” in ENVI command line input window. For the second case, users have to embed “AftAutoSpecUnmix” into ENVI first, then run it through ENVI user interface.

Once “AftAutoSpecUnmix” is launched, users are first prompted to input the image file to be processed and endmember spectral file if available. Then the users are required to select an unmixing algorithm and input other information related to spectral unmixing results, such as output endmember fraction image file name and extracted endmember spectral file name, etc. No further interaction is required. The extracted endmember spectra will be saved as a text file and displayed as spectral profiles. The endmember fractions will be saved in standard ENVI BSQ format and loaded into ENVI file input window.

Chapter 8

Conclusions and Future Work

Hyperspectral remote sensing technology enables us to use hyperspectral remote sensing imagery for ground cover material identification and discrimination with the technique called spectral unmixing. Among the spectral unmixing studies, linear spectral unmixing has drawn a lot of attention. The principle of the linear spectral unmixing assumes that there are a limited number of land cover materials (endmembers) existing in an image scene. These endmember spectra constitute the basic components of the image. Under this assumption, the spectra extracted from image pixels are thought of as the spectral mixture of the endmember spectra occurring in the image scene. Mathematically, these mixed pixel spectra are then expressed as the linear combination of the endmember spectra. The coefficients of each term in this combination represent the fractional abundance of the corresponding endmembers. Therefore finding the endmember abundance of each pixel, often called spectral unmixing, turns out to be a problem of solving a linear system.

The linear spectral unmixing has several variants, based on how much *a priori* information we have about the endmember spectra and whether we consider the constraints on the endmember abundant fractions. Starting from the simplest and unrealistic case, in which we need to know all the endmembers and do not consider any constraints, to the most complex and realistic situation, in which we do not know anything about the endmembers and take all the constraints into consideration, the linear

spectral unmixing variants are listed in the following table. Case s3 and 4 are chosen to be studied and implemented in this thesis, for they are closest to the real situation.

Table 8.1 Linear Spectral Unmixing Cases

Unmixing Cases	Endmember Spectra Required	Constraints Considered
1. Supervised and Unconstrained	Yes	No
2. Supervised and Constrained	Yes	Yes
3. Unsupervised and Unconstrained	No	No
4. Unsupervised and Constrained	No	Yes

For case 3, unsupervised and unconstrained, an unmixing algorithm based on the Constrained Energy Minimization (CEM_SUA) is introduced and implemented. It is tested with simulated hyperspectral data, and Hyperion and AVIRIS imagery. The results show that CEM_SUA works well in normal situations. The obtained endmember abundances are close to the known truth. But when the data signal-to-noise ratio (SNR) drops below 40, it fails to detect the endmembers with less abundance proportions, say below 20%. It is found that the global covariance matrix in CEM_SUA is the cause of the problem. To solve this problem, an improved version of CEM_SUA, LCEM_SUA, is derived by considering image spatial variability, in which several local covariance matrices are used to replace the single global one in CEM_SUA. It is demonstrated that LCEM_SUA has a better ability to distinguish weak target endmembers from a noisy background. Because CEM_SUA or LCEM_SUA needs target endmember spectra *a priori*, they are appropriate for the detection of a small number of target endmembers.

Though CEM_SUA and LCEM_SUA unmixing results are reasonable, they are not optimal, for they do not consider any constraints, ASC and ANC, on endmember abundance fractions. The unmixing result may be negative or greater than one. To

mitigate this problem, we introduce an unsupervised and constrained spectral unmixing algorithm (FCLS_SUA), which is case 4 in Table [8.1]. There are two steps involved in FCLS_SUA: first extract the endmember spectra, and then compute their abundance proportions. Here we employ the unconstrained least squares estimation to extract the endmember spectra directly from the image. The difference between each pixel value and its least squares estimation is computed. The pixel having the largest difference is selected as an endmember candidate, and is added to the endmember matrix. Once all the endmember spectra are determined, the spectral unmixing is performed based on the fully constrained least squares method, in which the ASC is considered by the Lagrange multiplier and the ANC is taken care of by a steering vector which locates the unqualified endmember spectra, removes them from the endmember matrix, and sets their abundance fractions to zero. FCLS_SUA is also tested with the simulated hyperspectral data, Hyperion, and AVIRIS imagery. The unmixing results are better than that of CEM_SUA or LCEM_SUA. Because FCLS_SUA is capable to finding endmembers from the images, it is suitable for natural resources endmember detection.

An automatic hyperspectral unmixing software is developed based on LCEM_SUA and FCLS_SUA, which has the flavor of the commercial remote sensing software with a graphical user interface, event-driven, and on-line help. This software is programmed in IDL, which can be used as either a stand-alone or a plug-in spectral unmixing program to ENVI. Compared with the off-the-shelf spectral unmixing software, such as ENVI, This program minimizes the user intervention and makes the spectral unmixing easier and

quicker. The program is being used at the Advanced Forest Technologies Laboratory of the Pacific Forestry Centre, Canadian Forest Service, Natural Resources Canada.

Linear spectral unmixing assumes that there only exists single scattering between photons of electromagnetic wave and ground materials. For tall vegetation, such as forest and crops, this assumption may not be true. Photons can penetrate vegetation canopy, bounce back and forth in the sub-layer of the vegetation, and then are reflected to sensors. This is a multi-scattering process. To accurately model this process, we need to describe it in terms of non-linear expressions. Therefore, the non-linear spectral unmixing is a practical problem, especially for hyperspectral applications on forest. Another interesting area is the combination of spectral unmixing and bidirectional reflectance distribution function (BRDF). It has been noted that an endmember spectrum changes with different viewing and illuminating angles. To accurately determine the endmembers and their abundance fractions in an image, therefore, we need to consider the viewing and illuminating geometry, which makes the spectral unmixing problem even challenging.

Bibliography

1. Barry, P., EO-1 Hyperion Science Data User's Guide, Level 1_B.
2. Bateson A., Curtiss B., A Method for Manual Endmember Selection and Spectral Unmixing, *Remote Sens. Environ.* Vol. 55 p229, (1996).
3. Boardman, J.W., "Inversion of High Spectral Resolution Data," *Proceedings of SPIE Conference on Imaging Spectrometry of the Terrestrial Environment*, Orlando, Florida, Vol. 1298, pp. 222-233, 1990.
4. Boardman, J. W., 1993, Automated spectral unmixing of AVIRIS data using convex geometry concepts: in *Summaries, Fourth JPL Airborne Geoscience Workshop*, JPL Publishing 93-26, v. 1, p. 11-14.
5. Boardman J. W., Analysis, understanding and visualization of hyperspectral data as convex sets in n-space, *Proceedings of the International SPIE Symposium on Imaging Spectrometry*, SPIE vol. 2480, p14 (1995).
6. Boardman J. W., Kruse F. A., Green R. O., Mapping target signatures via partial unmixing of AVIRIS data, *Proceedings of the 5th Annual JPL Airborne Earth Science Workshop*, Jet Propulsion Laboratory, Pasadena, California, USA, JPL Publication 95-1, p23, vol. 1, (1995).
7. Chang, C-I., Target Signature-Constrained Mixed Pixel Classification for Hyperspectral Imagery, *IEEE Transaction on Geoscience and Remote Sensing*, Vol. 40, No. 5. May 2002.
8. Chang, C-I., Du, Q., Chiang, S-S., Heinz, D., and Ginsberg, I., W., Unsupervised Target Subpixel Detection in Hyperspectral Imagery, *Proceedings of SPIE*, Vol. 4381, 2001.

9. Chang, C-I, Constrained Subpixel Target Detection for Remote Sensed Imagery, IEEE Transactions on Geoscience and Remote Sensing, Vol. 38, No. 3. May 2000.
10. Chrien, T. G., Green, R. O., and Eastwood, M. L., 1990, Accuracy of the spectral and radiometric laboratory calibration of the Airborne Visible/Infrared Imaging, Technical Report.
11. Craig M., Unsupervised unmixing of remotely sensed images, Proceedings of the Fifth Australian Remote Sensing Conference, p324, Perth, Western Australia, October, (1990).
12. Endsley N. H., Spectral unmixing algorithms based on statistical models, Proceedings of the International SPIE Symposium on Imaging Spectrometry, SPIE Vol. 2480, p23, (1995).
13. ENVI Programmer's Guide, September, 2000 Edition, Research Systems, Inc.
14. ENVI User's Guide, September, 2000 Edition, Research Systems, Inc.
15. Fanning D. W., IDL programming Techniques, 2nd Edition, Fanning Software Consulting, 2000.
16. Goetz, A. F. H., Vane, G., Solomon, J.E., and Rock, B. N., 1985, Imaging spectrometry for Earth remote sensing: Science, v.211, p. 1147 – 1153.
17. Goodenough, David G., A. S. (Pal) Bhogal, Andrew Dyk, Olaf Niemann, Tian Han, Hao Chen, Chris West, and Chris Schmidt 2001, "Calibration of Forest Chemistry for Hyperspectral Analysis," Proc. IGARSS 2001, Vol. 1, pp. 52-56, Sydney, Australia, July.

18. Green A. A., Berman M., Switzer P., M. D. Craig, A Transformation for Ordering Multispectral data in terms of Image Quality with Implications for Noise Removal, IEEE Trans. On Geoscience and Remote Sensing, P 295, vol. 28, (1990).
19. Gruninger J., Sundberg R. L., Bounds on component spectra of multispectral images, Proceedings of the SPIE Conference on Algorithms for Multispectral and Hyperspectral Imagery 3. Orlando, Florida, April, (1997).
20. Han, T, Goodenough, D., Dyk, A., and Love, J. Detection And Correction of Abnormal Pixels in Hyperion Images, Proceedings of IGARSS 2002, Volume III, pp. 1327 – 1330.
21. Harsanyi, J. C., and Chang, C. I., 1994, Hyperspectral image classification and dimensionality reduction: An orthogonal subspace projection approach: IEEE Trans. Geoscience And Remote Sens., V.32, p. 779 – 785.
22. Haskell K. H., Hanson R. J., An algorithm for linear least squares problems with equality and non-negativity constraints, Mathematical Programming, p98, vol. 21 (1981).
23. Heinz, D, Chang, C-I, and Althouse M., Fully Constrained Least-Squares Based Linear Unmixng, Proceedings of IGARSS 1999, Hamburg, Vol. 2, 1401 - 1403.
24. Hsuan R. and Chang C-I., A Generalized Orthogonal Subspace Projection Approach to Unsupervised Multispectral Image Classification, IEEE Transactions on Geoscience and Remote Sensing, Vol. 38, No. 6. November 2000, 2515 - 2528.
25. Kerekes, J. P. and Baum J. E., Spectral Imaging System Analytical Model for Subpixel Object Detection, IEEE Transactions on Geoscience and Remote Sensing, Vol. 40, No. 5. May 2002, 1088 - 1101.

26. Kruse, F. A., Lefkoff, A. B., Boardman, J. W., Heidebrecht, K. B., Shapiro, A. T., Barloon, J. P., and Goetz, A. F. H., 1993, The spectral image processing system (SIPS) – Interactive visualization and analysis of imaging spectrometer data: Remote Sensing of Environment, V.44, pp.145 – 163.
27. Kruse, F. A., Raines, G. L., and Watson, K., 1985, Analytical techniques for extracting geologic information from multichannel airborne spectroradiometer and airborne imaging spectrometer data: in Proceedings, 4th International Symposium on Remote Sensing of Environment, Thematic Conference on Remote Sensing for Exploration Geology, Environmental Research Institute of Michigan, Ann Arbor, p. 309 – 324.
28. Landgrebe, D., Hyperspectral Image Data Analysis, IEEE Signal Processing Magazine, Vol. 19, Jan. 2002, 17 - 28.
29. Lawson C. L., Hanson R. J., Solving Least Squares Problems, Prentice-Hall, Inc, Englewood Cliffs, N.J.,1974
30. Manidakis, D. and Shaw, G., Detection Algorithms for Hyperspectral Imaging Applications, IEEE Signal Processing Magazine, Vol. 19, Jan. 2002, 29 - 43.
31. Richards, J. A., Jia, X., Remote Sensing Digital Image Analysis – An Introduction 3rd Springer-Verlag Berlin 1999.
32. Porter, W. M., and Enmark, H. E., 1987, System overview of the Airborne Visible/Infrared Imaging Spectrometer (AVIRIS), in Proceedings, Society of Photo-Optical Instrumentation Engineers (SPIE), v.834, pp.22 – 31.
33. Press, W, Teukolsky, S., Vetterling, W. T., and Flannery, B. P., Numerical Recipes in C – the Art of Scientific Computing, Second Edition, Cambridge University Press. ISBN 0-521-43108-5, Cambridge, New York, 1992.

34. Price J. C., How Unique are Spectral Signatures?, *Remote Sens. Environ.*, vol. 49, p. 181, (1994).
35. Sasaki K., Kawata S., Minami S., Constrained nonlinear method for estimating component spectra from multi-component mixtures, *Applied Optics*, vol. 22, p. 3599, (1983).
36. Stein, D., Beaven, S. G., Hoff, L. E., Winter, E. M., Schaum, A. P, and Stocker A. D., Anomaly Detection from Hyperspectral Imagery, *IEEE Signal Processing Magazine*, Jan. 2002 [vol, pages, etc].
37. Vane, G., Green, R.O., Chrien, T.G., Enmark, H.T., Hansen, E.G., and Porter, W.M. , "The Airborne Visible/Infrared Imaging Spectrometer (AVIRIS)," *Remote Sensing of Environment*, Vol. 44, pp. 127-143, 1993.
38. WatKins, D. S., *Fundanmentals of Matrix Computations, Second Edition*, A John Wiley & Sons, Inc., Publication, New York, 2002.

Appendix A

Specifications of AVIRIS Image

The AVIRIS image used in this thesis was acquired on Aug. 10, 2001 over GVWD. The image has been fully radiometric corrected. The main specifications are summarized as follows:

Instantaneous Field of View (IFOV):	1 mrad
Ground Resolution:	20 m at 20,000 m
Total Scan Angle:	30°
Swath Width:	10.6 km at 20,000m
Spectral Coverage:	410 – 2450 nm
Pixels / Scan Line:	614
Number of Spectral Bands:	224
Number of Spectrometers Used:	4
Spectral Coverage of Each Spectrometer:	
Spectrometer A	410 – 700 nm
Spectrometer B	680 – 1270 nm
Spectrometer C	1250 – 1860 nm
Spectrometer D	1840 – 2450 μ m
Sampling Interval of Each Spectrometer:	
Spectrometer A	9.4 nm
Spectrometer B	9.4 nm
Spectrometer C	9.7 nm
Spectrometer D	9.7 nm
Scale factor:	1000 (band 1 – 160) 500 (band 161 – 224)
Offset:	0
Digitization:	10-bits
Data Rate:	17 mbps

Appendix B

Specification of Hyperion Image

The Hyperion image used in this thesis was acquired on Sept. 10, 2001 over GVWD. The image is processed at level 1b1, which is partially radiometric corrected. The main specifications are summarized as follows:

Instantaneous Field of View (IFOV):	0.043 mrad
Ground Resolution:	30 m
Swath Width:	7.65 km
Spectral Coverage:	357 – 2576 nm
Pixels / Line:	256
Number of Spectral Bands:	242
Number of Spectrometers Used:	2
Spectral Coverage of Each Spectrometer:	
Spectrometer 1 (VNIR)	357 – 1000 nm
Spectrometer 2 (SWIR)	900 – 2576 nm
Sampling Interval of Each Spectrometer:	
Spectrometer 1	10.08 nm
Spectrometer 2	10.12 nm
Scale factor:	40 (VNIR bands) 80 (SWIR bands)
Offset:	0
Digitization:	12-bits

Appendix C

Hyperion Level 1B1 Data Pre-processing

The Hyperion data are corrected by TRW and distributed at different processing levels. The highest version is level 1b1, which became effective 15 November 2001. The Hyperion level 1b1 dataset is generated from level 0 datasets through several processing steps including: smear correction, echo correction, background removal, radiometric correction, bad pixel repair, and image quality checking. Before the image can be used for spectral unmixing, two more corrections are required – destriping and desmiling.

1. Stripe and De-striping

The vertical stripes in Hyperion data are apparent, especially in the first 12 VNIR bands and many SWIR bands. It is believed that the Hyperion stripes are caused by the unbalanced detector array, because Hyperion system acquires data in pushbroom mode, in which there is a separate detector to gather data for each column of the image. If the detectors are not calibrated properly, striping artifacts could easily be generated.

A program is written to detect and correct these striping pixels. The algorithm is as follows. First the program reads in an image cube by spatial tiling, then traverses each band horizontally to compare each pixel's DN value with that of its immediate left and right neighboring pixels. If the pixel's DN value is smaller than the DN values of both neighbors, this pixel is labeled as abnormal. After abnormal pixel labeling, the program traverses each band vertically to count the number of consecutive abnormal pixels and the total number of pixels in each column. If the number of the consecutive abnormal pixels is greater than a user-defined-threshold-value (the longest vertical ground feature in pixels) and if the percentage of abnormal pixels in the column is greater than another user-defined-threshold-value (usually 50%), then the pixels in the column are marked as abnormal pixels, and their locations are recorded in another image file. The final step is to correct the abnormal pixels by replacing their DN values with the average DN values of their immediate left and right neighboring pixels.

2. Smile and De-smiling

The smile refers to the cross-track spectral error, which exists in all levels of Hyperion datasets. Smile is caused by the cross-track detector spectral shift with detector location. According to the Hyperion ground spectral calibration results provided by TRW, the shifts are dependent on the pixel position across track and wavelength. For VNIR bands, the shifts range between 2.6 and 3.6 nm. The maximum shift happens at pixel 256 of band 1. For the SWIR bands, the shifts are within 1 nm.

The smile effect is not shown in image space, but it can be visualized in eigenvector space, where it appears as a brightness gradient across track. The smile is caused by the wavelength shift away from the nominal center wavelength, so it can be corrected by shifting it back. Starting with the Hyperion ground spectral calibration data from TRW, we wrote a program to correct the smile based on polynomial curve fitting and interpolation. The Hyperion data used in this thesis have been de-striped and de-smiled.

VITA

Surname: Han

Given Names: Tian

Place of Birth: Nanpi, Hebei, China

Educational Institutions Attended:

University of Victoria

2000 – 2002

Ocean University of Qingdao

1980 – 1984

Degrees Awarded:

B.Sc.

Ocean University of Qingdao

1984

Publications:

Han, T. and Goodenough, D. G., Hyperspectral Endmember Detection and Unmixing Based on Linear Programming, Processings of IGARSS 2003, accepted.

Han, T. and Goodenough, D. G., Detection and Correction of Abnormal Pixels in Hyperion Images, Proceedings of IGARSS 2002, Volume III, pp.1327 – 1330.

UNIVERSITY OF VICTORIA PARTIAL COPYRIGHT LICENSE

I hereby grant the right to lend my thesis (or dissertation) to users of the University of Victoria Library, and to make single copies only for users or in response to a request from the Library of any other university, or similar institution, on its behalf or for one of its users. I further agree that permission for extensive copying of this thesis for scholarly purposes may be granted by me or a member of the University designated by me. It is understood that copying or publication of this thesis for financial gain by the University of Victoria shall not be allowed without my written permission.

Title of Thesis / Dissertation:

An Automatic System for Hyperspectral Remote Sensing Endmember Unmixing

Author:



Tian Han

April 30, 2003